AIAA JOURNAL
Vol. 44, No. 4, April 2006

Subgrid Modeling for Simulation of Spray Combustion in Large-Scale Combustors

Suresh Menon* and Nayan Patel†
Georgia Institute of Technology, Atlanta, Georgia 30332

Simulations of spray combustion in full-scale combustors under different operating conditions are conducted using large-eddy simulations (LES). The current methodology attempts to capture not only spray-turbulence interactions but also subgrid fuel–air mixing and finite-rate kinetics occurring at scales below the LES resolution. Reduced finite-rate kinetics for n-heptane and kerosene fuels are used in these studies to predict pollutant emission. Comparison of LES predictions with measurements for a single-cup swirl combustor shows reasonably good agreement. Results for spray combustion in a realistic two-cup combustor sector show a complex vortex breakdown process that creates multiple recirculation regions in the combustor. These regions of recirculation provide multiple sites to stabilize the spray and the flame. Because of the shape of the combustor, significant three-dimensional effects are apparent with no similarity between flame structures, vortex breakdown bubbles, and outflow between the two cups. Spray combustion is quite efficient during full power operation because of the distributed injection process. It is also shown that in the current subgrid mixing and combustion approach flame stabilization is more physical, and the flame anchors downstream of the dump plane. In contrast, a conventional LES study using a subgrid eddy breakup model shows a flame anchored inside the inlet, immediately downstream of the spray injector, which is unphysical.

Introduction

SWIRL stabilization of combustion is employed in all operational gas turbines[1] because of the ability of swirl to create an aerodynamic flame holder in the combustor. Swirling flow entering the combustor encounters an adverse pressure gradient, and this results in the formation of a vortex breakdown bubble (VBB) that provides an aerodynamic (i.e., nonphysical) barrier to the flow. Typically, the flame is stabilized upstream of this recirculating flow. Although the nature of this stabilization process has been known and exploited for some time, the dynamics of flame interaction with the swirling shear layers separating from the inlet and the VBB is not well understood, especially over a wide range of operating conditions. Flame stabilization by the VBB in a premixed system is substantially different than in liquid-fueled (spray) systems because in the latter system flame structure depends considerably on droplet vaporization and on the state of the mixedness of the vaporized fuel with the oxidizer in the vicinity of the VBB.

The current trend in next-generation gas-turbine engine design is toward lean combustion for a variety of reasons, including the need to increase fuel efficiency and reduce pollutant emission. However, as combustion approaches the lean flammability limit, small local perturbation in flow and/or fuel equivalence ratio can lead to local extinction and to rapid increase in CO emission. Global flame extinction [also known as lean blowout (LBO)] can also occur.

LBO has been observed not only in premixed systems but also in liquid-fueled combustors and, thus, is an issue of concern in all operational combustors. Experimental studies[2] show that an exponential increase in CO emission level occurs as the system approaches the LBO limit. This is likely caused by local quenching of the flame in the highly unsteady turbulent regions, which releases unburned hydrocarbons (UHC) into the postflame region that subsequently oxidizes into CO (Ref. 3). In liquid-fueled systems, LBO is also probably affected by droplet residence and vaporization timescales, in addition to mixing time. Predicting engine performance near LBO in both gas-fueled (i.e., premixed) and liquid-fueled gas turbines is currently a major research effort.

Combustion instability is another area of considerable concern for all gas turbine engines, especially in the lean limit. As the combustion process approaches the lean flammability limit, the flame becomes susceptible to small perturbations inside the combustion chamber. These perturbations manifest themselves as pressure oscillations and perturb the fuel feeding system causing spatial inhomogeneity in the incoming reactant mixture. These inhomogeneities can modify the heat-release pattern, which, in turn, can trigger pressure (acoustic) fluctuations. Unsteady heat release in phase with the pressure oscillation can lead to large-amplitude, low-frequency pressure oscillation. These oscillations can lead to combustion instability that can be catastrophic.

LBO and combustion instability need not occur together nor do they have to be related to each other. For example, LBO can occur without exciting any acoustic modes. However, some of the underlying physics of the combustion process near LBO and during combustion instability are similar because both processes involve nonlinear coupling between shear flow and unsteady flame motion (and heat release). Experimental studies[4] of combustion instability and/or LBO in both premixed and spray combustion systems have obtained the overall system response and exhaust emission data. However, the details of the local flame dynamics in the highly swirling flow and the local extinction characteristics are almost impossible to obtain in experimental rigs. Furthermore, most laboratory rigs operate at atmospheric pressure, whereas operational combustors operate at high pressure. Thus, many of finer details needed to understand how acoustic-vortex-flame interactions control the combustion process near LBO and/or during instability under realistic conditions have been very difficult to obtain.

Computational studies can offer another capability to investigate such complex processes. A "validated" computational study might be a much more cost-effective approach to study the underlying physics because all flow properties are available in space and time. Because of the inherent unsteadiness of all of the important processes, both spatial and time accuracy is essential in the simulation strategy. Because direct numerical simulations is not feasible for such complex flows, only large-eddy simulation (LES) has the potential of addressing all of these concerns. This paper uses the LES

Presented as Paper 2004-0157 at the 42nd Aerospace Sciences Meeting, Reno, NV, 5–8 January 2004; received 30 November 2004; revision received 12 August 2005; accepted for publication 22 September 2005.

*Professor, School of Aerospace Engineering. Associate Fellow AIAA.
†Graduate Student, School of Aerospace Engineering.

approach to simulate liquid-fueled combustion in a sector rig under realistic conditions.

Other issues, more specific to the combustion process, also must be considered for LES modeling. It has been shown earlier[5,6] that premixed gas turbines (e.g., GE LM6000, DOE-HAT) operate in the thin-reaction-zone (TRZ) regime,[7] where the smallest turbulent scales can penetrate into the flame structure and thicken it (even though the actual reaction zone is thin). However, as the system approaches the LBO limit, the conditions tend toward the broken-reaction-zone (BRZ) regime, where there is no discernible contiguous flame structure. Thus, the LES methodology must be able to deal with both TRZ and BRZ regimes (as well as, the corrugated flamelet regime) without requiring ad hoc changes to the model (because all these regimes can and do coexist in the combustor).

Recent studies[3,6] have shown that flamelet models have limited validity in BRZ regime. An alternate approach that employs a subgrid mixing and combustion model was shown to have a more general applicability in all combustion regimes without requiring any model adjustment. This paper follows this same strategy for liquid-fueled systems because the local state of mixedness in a spray combustion system can range from completely nonpremixed, to partially premixed to fully premixed state.

This paper describes a LES approach to study liquid-fueled combustion. A subgrid mixing model called the linear-eddy-mixing (LEM) model[8–10] is implemented in LES. (This combined approach is called LEMLES, hereafter.) Past studies of scalar mixing,[11,12] nonpremixed combustion,[13,14] premixed combustion,[15–19] and two-phase spray mixing and combustion[20–23] have shown that the LEM model can handle scalar mixing and combustion under a wide range of conditions.

This paper is organized as follows. In the next section, we describe the LES formulation for two-phase flow and the subgrid models used in this study. In the third section we summarize the numerical approach and the test problems simulated. This is followed by the fourth section that describes all of the results obtained in this study. Finally, in the last section we discuss the key conclusions of this study and the unresolved issues that warrant further investigation.

Formulation

In this section, we briefly describe the LES model to establish the methodology used in the current study. More details are given in cited references.

LES Equations

The governing equation of motion for an unsteady, compressible, reacting, multispecies fluid is employed in this study. The compressible approach is used here to capture the coupling between pressure oscillations (acoustic wave motion), vorticity dynamics, and combustion heat release. This coupling must be properly resolved at all relevant scales in order to predict the physics near LBO and during combustion instability.[24] The LES approach for spray modeling uses the Eulerian–Lagrangian approach in which the gas-phase equations are solved on an Eulerian grid while the droplets are tracked using a Lagrangian approach.[25] Full two-way coupling is carried out, as described next.

The flow variables are decomposed into the resolved and unresolved (subgrid-scale) components by a spatial filtering operation, such that $f = \tilde{f} + f''$, where the tilde $\sim$ denotes resolved scale and double prime $''$ denotes unresolved subgrid scale quantities. The Favre filtered variable is defined as $\tilde{f} = \overline{\rho f}/\bar{\rho}$, where the overbar represents a spatial filtering.[26]

Applying the filtering to the conservation equations results in the following LES equations for the gas phase:

$$\frac{\partial \bar{\rho}}{\partial t} + \frac{\partial \bar{\rho}\tilde{u}_i}{\partial x_i} = \widetilde{\dot{\rho}_s} \tag{1}$$

$$\frac{\partial \bar{\rho}\tilde{u}_i}{\partial t} + \frac{\partial}{\partial x_j}\left[\bar{\rho}\tilde{u}_i\tilde{u}_j + \bar{p}\delta_{ij} - \bar{\tau}_{ij} + \tau_{ij}^{\text{sgs}}\right] = \widetilde{F_{s,i}} \tag{2}$$

$$\frac{\partial \bar{\rho}\tilde{E}}{\partial t} + \frac{\partial}{\partial x_i}\left[(\bar{\rho}\tilde{E} + \bar{p})\tilde{u}_i + \bar{q}_i - \tilde{u}_j\bar{\tau}_{ji} + H_i^{\text{sgs}} + \sigma_i^{\text{sgs}}\right] = \widetilde{\dot{Q}_s} \tag{3}$$

$$\frac{\partial \bar{\rho}\tilde{Y}_k}{\partial t} + \frac{\partial}{\partial x_i}\left[\bar{\rho}\tilde{Y}_k\tilde{u}_i + \bar{\rho}\widetilde{Y_k V_{i,k}} + Y_{i,k}^{\text{sgs}} + \theta_{i,k}^{\text{sgs}}\right] = \bar{\dot{w}}_k + \widetilde{\dot{S}_{s,k}} \qquad k = 1, \ldots, N_s \tag{4}$$

Here N_s is the total number of species present in the system. In the preceding equations, all terms with superscript sgs denote subgrid quantities that require closure, and all terms on the right-hand side with subscript s are the source terms from the liquid phase (described next). Here ρ, u_i, Y_k, and $\dot{w}_k$ are, respectively, the mixture density, the velocity, the kth species mass fraction, and the reaction rate for the kth species. Also, $\bar{\tau}_{ij}$ is the filtered viscous tensor (defined in terms of the filtered quantities), and $\bar{q}_i$ is the filtered heat-flux vector given by

$$\bar{q}_i = -\bar{\kappa}\frac{\partial \tilde{T}}{\partial x_i} + \bar{\rho}\sum_{k=1}^{N_s}\tilde{h}_k\tilde{Y}_k\widetilde{V_{i,k}} + \sum_{k=1}^{N_s}q_{i,k}^{\text{sgs}} \tag{5}$$

The filtered diffusion velocities are obtained using Fick's law: $\widetilde{V_{i,k}} = (-\bar{D}_k/\tilde{Y}_k)(\partial\tilde{Y}_k/\partial x_i)$, and $\tilde{h}_k$ is the filtered specific enthalpy for the kth species. In the preceding relations, $\bar{\mu}$, $\bar{\kappa}$, and $\bar{D}_k$ are, respectively, the filtered mixture molecular viscosity, mixture thermal conductivity, and kth species diffusion coefficient. These transport properties are determined as a function of the filtered quantities.

The pressure is determined from the filtered equation of state, $\bar{p} = \bar{\rho}\tilde{R}\tilde{T} + \bar{\rho}T^{\text{sgs}}$, and the filtered total energy per unit volume is $\bar{\rho}\tilde{E} = \bar{\rho}\tilde{e} + \frac{1}{2}\bar{\rho}\tilde{u}_i\tilde{u}_i + \bar{\rho}k^{\text{sgs}}$. Here

$$\tilde{R} = \sum_{k=1}^{N_s}R_k\tilde{Y}_k$$

is the mixture gas constant, R_k is the kth species gas constant, and the subgrid kinetic energy is defined as $k^{\text{sgs}} = (1/2)[\widetilde{u_k u_k} - \tilde{u}_k\tilde{u}_k]$. The filtered internal energy for calorically perfect gases is given by

$$\tilde{e} = \sum_{k=1}^{N_s}[c_{v,k}\tilde{Y}_k\tilde{T} + \tilde{Y}_k\Delta h'_{f,k}]$$

where $\Delta h'_{f,k} = \Delta h^0_{f,k} - c_{p,k}T^0$ and $\Delta h^0_{f,k}$ is the standard heat of formation at a reference temperature T^0. The current LEMLES also has an option to simulate thermally perfect gas.

The subgrid terms that require closure are

$$\tau_{ij}^{\text{sgs}} = \bar{\rho}(\widetilde{u_i u_j} - \tilde{u}_i\tilde{u}_j) \tag{6}$$

$$H_i^{\text{sgs}} = \bar{\rho}(\widetilde{Eu_i} - \tilde{E}\tilde{u}_i) + (\overline{pu_i} - \bar{p}\tilde{u}_i) \tag{7}$$

$$\sigma_i^{\text{sgs}} = \widetilde{u_j\tau_{ij}} - \tilde{u}_j\bar{\tau}_{ij} \tag{8}$$

$$Y_{i,k}^{\text{sgs}} = \bar{\rho}[\widetilde{u_i Y_k} - \tilde{u}_i\tilde{Y}_k] \tag{9}$$

$$q_{i,k}^{\text{sgs}} = \left[\overline{h_k D_k \partial Y_k/\partial x_i} - \tilde{h}_k\tilde{D}_k\partial\tilde{Y}_k/\partial x_i\right] \tag{10}$$

$$\theta_{i,k}^{\text{sgs}} = \bar{\rho}[\widetilde{V_{i,k}Y_k} - \tilde{V}_{i,k}\tilde{Y}_k] \tag{11}$$

$$T^{\text{sgs}} = \sum_{k=1}^{N_s}R_k[\widetilde{Y_k T} - \tilde{Y}_k\tilde{T}] \tag{12}$$

in addition to the filtered reaction-rate term $\bar{\dot{w}}_k$.

Momentum Transport Closure

The subgrid-stress tensor τ_{ij}^{sgs} is closed using a subgrid eddy viscosity and a gradient diffusion model at the grid cutoff scale:

$$\tau_{ij}^{\text{sgs}} = -2\bar{\rho}\nu_t\left[\tilde{S}_{ij} - \tfrac{1}{3}\tilde{S}_{kk}\delta_{ij}\right] + \tfrac{2}{3}\bar{\rho}k^{\text{sgs}}\delta_{ij} \tag{13}$$

Here, the resolved rate of strain is given as $\tilde{S}_{ij} = (1/2)(\partial\tilde{u}_i/\partial x_j + \partial\tilde{u}_j/\partial x_i)$, and the subgrid eddy viscosity is ν_t. Because large-scale motion is resolved in LES, the associated countergradient effects at the large scales are also resolved (even though a gradient closure is employed for τ_i^{sgs} at the grid cutoff scale).

To obtain ν_t and k^{sgs}, a nonequilibrium model[27,28] for the subgrid kinetic energy k^{sgs} is used and is given by

$$\frac{\partial\bar{\rho}k^{\text{sgs}}}{\partial t} + \frac{\partial}{\partial x_i}\left(\bar{\rho}\tilde{u}_i k^{\text{sgs}}\right) = -\tau_{ij}^{\text{sgs}}\frac{\partial\tilde{u}_i}{\partial x_j} - C_\epsilon\bar{\rho}\frac{(k^{\text{sgs}})^{\frac{3}{2}}}{\bar{\Delta}} + \frac{\partial}{\partial x_i}\left(\bar{\rho}\frac{\nu_t}{C_t}\frac{\partial k^{\text{sgs}}}{\partial x_i}\right) + F_d \tag{14}$$

In the preceding equation, $F_d = \widetilde{u_i F_{s,i}} - \tilde{u}_i\widetilde{F_{s,i}}$ is the source term caused by the particle phase. (This term can be closed exactly, as shown earlier.[20]) The subgrid eddy viscosity is modeled as $\nu_t = C_\nu\bar{\Delta}\sqrt{k^{\text{sgs}}}$, where $\bar{\Delta} = (\Delta x\Delta y\Delta z)^{1/3}$ is based on local grid size $(\Delta x, \Delta y, \Delta z)$. There are three coefficients in the preceding closure coefficients, C_ν, C_ϵ, and C_t. The nominal "constant" values for these coefficients are[11,15] 0.067, 0.916, and 1.0, respectively.

However, in this study these coefficients are obtained by using a localized dynamic procedure for the subgrid kinetic energy model[29,30] (denoted as LDKM, hereafter). This dynamic procedure uses the experimental observation in high-Reynolds-number turbulent jet[31] that the subgrid-stress τ_{ij}^{sgs} at the grid filter level $\bar{\Delta}$ and the Leonard's stress $L_{ij}(= [\langle\bar{\rho}\widetilde{u_i}\widetilde{u_j}\rangle - \langle\bar{\rho}\tilde{u}_i\rangle\langle\bar{\rho}\tilde{u}_j\rangle]/\hat{\bar{\rho}})$ at the test filter level $\hat{\Delta}(=2\bar{\Delta})$ are self-similar. Here (and henceforth), $\langle f\rangle$ and $\hat{f}$ both indicate test filtering. Because L_{ij} can be explicitly computed at the test filter level, a simple scale-similar model of the form $\tau_{ij}^{\text{sgs}} = C_L L_{ij}$, where C_L is an adjustable constant, was proposed earlier[31] but was found to lack proper dissipation.

In the LDKM model, the preceding observation is extended, and it is assumed that L_{ij} and the subgrid stress $\hat{\tau}_{ij}^{\text{sgs}}$ at the test filter level are also similar (i.e., $\hat{\tau}_{ij}^{\text{sgs}} = \widehat{C_L}L_{ij}$). Using this, $\hat{\tau}_{ij}^{\text{sgs}}$ is modeled using the same form as for τ_{ij}^{sgs} [Eq. (13)], except that all variables are defined at the test filter level. We define the subgrid kinetic energy at the test filter level as $k_{\text{test}} = \frac{1}{2}[\widehat{\bar{\rho}\tilde{u}_k^2}/\hat{\bar{\rho}} - \widehat{\bar{\rho}\tilde{u}_k}^2/\hat{\bar{\rho}}^2]$ and obtain a relation

$$L_{ij} = \hat{\tau}_{ij}^{\text{sgs}}/\widehat{C_L} = -2\hat{\bar{\rho}}(C_\nu/\widehat{C_L})\sqrt{k_{\text{test}}}\hat{\Delta}\left(\langle\widetilde{S_{ij}}\rangle - \tfrac{1}{3}\langle\widetilde{S_{kk}}\rangle\delta_{ij}\right) + \tfrac{2}{3}\left(1/\widehat{C_L}\right)\hat{\bar{\rho}} \sim k_{\text{test}}\delta_{ij} \tag{15}$$

In the preceding equation, we assume $\widehat{C_L} = 1$, and so the only unknown is C_ν. This equation is, thus, an explicit model representation for the constant C_ν in terms of quantities resolved at the test filter level. This system of equations represents five independent equations for one unknown coefficient (and hence is an overdetermined system). The value of C_ν is determined in an approximated manner by applying the least-square method.[32] Thus,

$$C_\nu = -\frac{L'_{ij}M_{ij}}{2M_{ij}M_{ij}} \tag{16}$$

In the preceding expression

$$L'_{ij} = L_{ij} - \tfrac{2}{3}\hat{\bar{\rho}}k_{\text{test}}\delta_{ij} \tag{17}$$

$$M_{ij} = \hat{\bar{\rho}}\sqrt{k_{\text{test}}}\hat{\Delta}\left(\langle\tilde{S}_{ij}\rangle - \tfrac{1}{3}\langle\tilde{S}_{kk}\rangle\delta_{ij}\right) \tag{18}$$

A similar approach is used to obtain the dissipation coefficient C_ε such that

$$C_\epsilon = \frac{\hat{\Delta}(\mu+\mu_t)}{\hat{\bar{\rho}}k_{\text{test}}^{\frac{3}{2}}}\left[\left\langle\widetilde{T_{ij}}\frac{\partial\widetilde{u}_j}{\partial x_i}\right\rangle - \widehat{\widetilde{T}_{ij}}\frac{\widehat{\partial\widetilde{u}_j}}{\partial x_i}\right] \tag{19}$$

where μ is the molecular viscosity and $\mu_t(=\nu_t * \bar{\rho})$ is eddy viscosity at the grid filter level. The tensor $\widetilde{T}_{ij}$ is defined as $[\partial\widetilde{u}_i/\partial x_j + \partial\widetilde{u}_j/\partial x_i - \frac{2}{3}(\partial\widetilde{u}_k/\partial x_k)\delta_{ij}]$ and $\widehat{\widetilde{T}}_{ij}$ indicates tensor at the test-filter level.

More details are given elsewhere.[29,30] There are a few noteworthy points to highlight in this closure: 1) the LDKM approach does not employ the Germano's identity[33]; 2) the self-similar approach implies that both $\bar{\Delta}$ and $\hat{\Delta}$ must lie in the inertial range, and this provides a (albeit) rough estimate for the minimum grid resolution that can be used for a given Reynolds number; 3) the denominators in both Eqs. (16) and (19) are well-defined quantities at the test filter level and can be directly computed; 4) the evaluation of the coefficients can be carried out locally (i.e., at all grid points) in space without encountering any instability; 5) the LDKM approach satisfies all of the realizability conditions[34] in the majority of the grid points even in complex swirling reacting flows; and 6) the dynamic evaluation can be used near walls without any change.[35,36] Finally, the computational overhead of the LDKM is not very significant because only one additional equation has to be solved.

Energy and Scalar Transport Closure

In addition to τ_{ij}^{sgs}, other subgrid terms that appear in the LES filtered energy and species equations have to be closed. The subgrid total enthalpy flux H_i^{sgs} is also modeled using the eddy viscosity and a gradient assumption as

$$H_i^{\text{sgs}} = -\bar{\rho}\frac{\nu_t}{Pr_t}\frac{\partial\tilde{H}}{\partial x_i} \tag{20}$$

Here $\tilde{H}$ is the filtered total enthalpy, and Pr_t is a turbulent Prandtl number that can also be computed using a dynamic procedure but is currently assumed to be unity. The total enthalpy term $\tilde{H}$ is evaluated as sum of specific enthalpy of mixture, specific kinetic energy, and specific subgrid-scale energy: $\tilde{H} = \tilde{h} + \tilde{u}_i\tilde{u}_i/2 + k^{\text{sgs}}$, where

$$\tilde{h} = \sum_{k=1}^{N}\tilde{h}_k\tilde{Y}_k$$

In conventional LES [i.e., methods that solve the filtered species equations, Eq. (4) along with the filtered Navier–Stokes equations], the subgrid convective species flux $Y_{i,k}^{\text{sgs}}$ is modeled using the gradient diffusion assumption, as well. Thus,

$$Y_{i,k}^{\text{sgs}} = -\frac{\bar{\rho}\nu_t}{Sc_t}\frac{\partial\tilde{Y}_k}{\partial x_i} \tag{21}$$

The coefficient Sc_t is the turbulent Schmidt number and is taken to be unity but could be computed dynamically. The gradient closure for the species subgrid flux is more problematic than for momentum or energy transport because scalar mixing and diffusion occur at the subgrid scale. Scalar structure is highly anisotropic at the small scales, and a subgrid gradient transport is not necessarily a correct or even a valid assumption.

The other unclosed terms such as σ_i^{sgs}, $q_{i,k}^{\text{sgs}}$, T^{sgs}, and $\theta_{i,k}^{\text{sgs}}$ are often neglected in conventional LES approaches,[37] but there is no clear justification. In the LEMLES approach (described in the next section), most of these terms are not neglected because of the nature of the model for subgrid scalar transport.

Subgrid Scalar Closure

In LEMLES, the filtered scalar equation (4) is not solved directly. Rather, molecular diffusion, small- and large-scale turbulent convection, and chemical reaction are all modeled separately, but concurrently at their respective timescales. To briefly describe this model mathematically, we split the velocity field as $u_i = \tilde{u}_i + (u'_i)^R + (u'_i)^S$. Here, $\tilde{u}_i$ is the LES-resolved velocity field, $(u'_i)^R$ is the LES-resolved subgrid fluctuation (obtained from k^{sgs}), and $(u'_i)^S$ is the unresolved subgrid fluctuation. Then, consider the exact species equation (i.e., without any explicit LES filtering) for the kth scalar Y_k written in a slightly different form as

$$\rho\frac{\partial Y_k}{\partial t} = -\rho\left[\tilde{u}_i + (u'_i)^R + (u'_i)^S\right]\frac{\partial Y_k}{\partial x_i} - \frac{\partial}{\partial x_i}(\rho Y_k V_{i,k}) + \dot{w}_k + \dot{S}_{s,k} \tag{22}$$

In LEMLES, the preceding equation is rewritten as

$$\frac{Y_k^* - Y_k^n}{\Delta t_{\text{LES}}} = -\left[\tilde{u}_i + (u_i')^R\right]\frac{\partial Y_k^n}{\partial x_i} \tag{23}$$

$$Y_k^{n+1} - Y_k^* = \int_t^{t+\Delta t_{\text{LES}}} -\frac{1}{\rho}\left[\rho(u_i')^S\frac{\partial Y_k^n}{\partial x_i} + \frac{\partial}{\partial x_i}(\rho Y_k V_{i,k})^n - \dot{w}_k^n - \dot{S}_{s,k}^n\right]\mathrm{d}t' \tag{24}$$

Here Δt_{LES} is the LES time step. Equation (23) describes the large-scale three-dimensional LES-resolved convection of the scalar field and is implemented by a Lagrangian transfer of mass across the finite volume cell surfaces.[13,15] Equation (24) describes the subgrid LEM model, as viewed at the LES space and timescales. The integrand includes four processes that occur within each LES grid and represent, respectively, 1) subgrid molecular diffusion, 2) reaction kinetics, 3) subgrid stirring, and 4) phase change of the liquid fuel. These processes are modeled on a one-dimensional domain embedded inside each LES grid where the integrand is rewritten in terms of the subgrid time- and space scales.

We first describe the subgrid processes in Eq. (24) and then the three-dimensional advection process in Eq. (23).

Subgrid Reaction-Diffusion Processes

Within each LES cell, the following one-dimensional reaction-diffusion model is solved:

$$\rho\frac{\partial Y_k^m}{\partial t^s} = F_s^m - \frac{\partial}{\partial s}\left(\rho Y_k^m V_{s,k}^m\right) + \dot{w}_k + \dot{S}_{s,k}^m \tag{25}$$

Here t^s indicates a local LEM timescale, and the superscript m indicates that the subgrid field within each LES cell is discretized by N_{LEM} number of subgrid cells along the local coordinate s, such that the LES-resolved quantity $\tilde{Y}_k$ is obtained by an Favre average of the subgrid field. Thus,

$$\tilde{Y}_k = \left(1\Big/\sum_{m=1}^{N_{\text{LEM}}}\rho^m\right)\sum_{m=1}^{N_{\text{LEM}}}(\rho Y_k)^m$$

The length of the LEM domain is equal to that of the local LES filter width $\bar{\Delta}$, and the number of LEM cells N_{LEM} is chosen so that all of the relevant scales are resolved. Typically, the smallest eddy (e.g., the Kolmogorov scale η) is resolved using six LEM cells, and η is estimated from the relation $\bar{\Delta}/\eta \approx Re_{\bar{\Delta}}^{3/4}$. Here, $Re_{\bar{\Delta}} = u'\bar{\Delta}/\nu$ is the local subgrid Reynolds number, and $u' = \sqrt{(2k^{\text{sgs}}/3)}$ is the subgrid turbulence intensity.

In real devices, N_{LEM} will vary from LES cell to cell because Re_{Δ} is a local variable; however, variable subgrid resolution requires significant modifications to the parallel solver to achieve proper load balancing. Therefore, in the present study the optimal N_{LEM} is chosen based on the resolution requirement in the primary region of interest (typically, regions of high shear flow where scalar mixing and combustion is occurring), and then the same LEM resolution is used in all LES cells. This allows proper load balancing at the expense of some redundant computations.

Equation (25) is solved using a standard finite difference scheme along the one-dimensional domain s. The time step for this integration Δt_{LEM} is determined as the minimum of the local diffusion Δt_{diff} or the chemical Δt_{chem} timescales. Inflow and outflow conditions to Eq. (25) are prescribed by the mass transport in the Lagrangian step, Eq. (23), and is further described next.

The inflow is prescribed at one end of the LEM domain and the outflow at the other end and is implemented by the splicing process described in the subgrid scalar transport subsection. Once this transport is completed, the finite difference of Eq. (25) is carried out using zero-gradient condition at each end. To maintain strict mass conservation, inflow-outflow by the splicing process occurs at every LES time step.

Detailed multicomponent kinetics can be included within this model using either direct integration or using in situ adaptive tabulation (ISAT).[38] Because all of the turbulent scales below the grid are resolved in this approach, both molecular diffusion and chemical kinetics are closed in an exact manner. As a result, "subgrid" terms such as $Y_{i,k}^{\text{sgs}}$, $q_{i,k}^{\text{sgs}}$, $\theta_{i,k}^{\text{sgs}}$, T^{sgs}, and $\bar{\dot{w}}_k$ do not have to be closed (nor do they actually exist in LEMLES) or modeled. In fact, it is possible to actually estimate these quantities from the simulated subgrid scalar fields.

The phase change of the liquid fuel into its gaseous form results in the source term in Eq. (25). This source term is determined from the Lagrangian solver, as described later.

The one-dimensional domain s in each LEM cell is not physically oriented along any of the Cartesian (x, y, or z) directions and is considered oriented in the direction of the local, instantaneous maximum scalar gradient.[8,10,15] The local flame shape or scalar field structure will vary from LES cell to cell and will also change in time because of mixing and combustion. Therefore, the local one-dimensional orientations will also change with the condition in each of the LES cells. The space- and time-varying orientation of these one-dimensional lines is an unique feature of the LEMLES approach and is implemented locally by the stirring process, as described next.

Subgrid Stirring

In the LEM domain, the effect of eddies smaller than the grid scale $\bar{\Delta}$ is physically accounted for as subgrid stirring. This effect is symbolically represented as F_s^m in Eq. (25) and represents the term

$$\int (u_i')^S\left(\frac{\partial Y_k^n}{\partial x_i}\right)\mathrm{d}t'$$

in Eq. (24). In the one-dimensional LEM domain, this three-dimensional term is approximated assuming locally isotropic conditions and is implemented using stochastic rearrangement events called *triplet maps*. Each triplet map[8] represents an instantaneous action of a three-dimensional (but isotropic) turbulent eddy on the subgrid scalar field. The mapping process is designed such that it compresses and increases the scalar gradient so that the local scalar field reflects the aforementioned orientation of the one-dimensional domain in the direction of the scalar gradient.

Because all scalar processes are resolved in a one-dimensional line, it is implicitly assumed that the turbulent scales involved in the stirring of the scalar fields are isotropic. This assumption is quite reasonable because it is consistent with LES approach, which assumes all scales below the grid scale are isotropic.

To implement this subgrid stirring, three parameters have to be prescribed: the local eddy size, the frequency of stirring, and the location of the stirring event within the LEM one-dimensional line. The eddy size l is picked randomly from an eddy size distribution $f(l)$ in the range $\bar{\Delta}$ to η (Kolmogorov scale), and stirring events occur at a specified frequency λ, and the location of this stirring event is chosen from a uniform distribution. Both $f(l)$ and λ are obtained using three-dimensional inertial-range scaling laws (for isotropic scales) derived from Kolmogorov's hypothesis as

$$\lambda = \frac{54}{5}\frac{\nu Re_{\bar{\Delta}}}{C_\lambda\bar{\Delta}^3}\frac{[(\bar{\Delta}/\eta)^{\frac{5}{3}} - 1]}{[1 - (\eta/\bar{\Delta})^{\frac{4}{3}}]} \tag{26}$$

C_λ is a constant determined to be 0.067 (Ref. 11). The eddy size l is chosen from the probability density function (PDF)

$$f(l) = \frac{(5/3)l^{-\frac{8}{3}}}{\eta^{-\frac{5}{3}} - \bar{\Delta}^{-\frac{5}{3}}} \tag{27}$$

where $\eta = N_\eta\bar{\Delta}Re_{\bar{\Delta}}^{-3/4}$. The empirical constant N_η reduces the effective range of scale between the integral length scale and η but does not change the turbulent diffusivity. Past studies have investigated the sensitivity of predictions to N_η, and we use $N_\eta = 11$ based on past studies.[39]

It has been demonstrated that the turbulent scaling laws predict correctly the growth of the flame surface area under the influence of turbulent strain. Note that this model does not require any change when the flame type (premixed, nonpremixed, or spray) or the combustion regime (flamelet, TRZ or BRZ regimes) changes. This ability has been demonstrated in the past,[3,17,19] and it is this ability that we believe is crucial to deal with combustion and flame dynamics as the system approaches LBO.

The LEM subgrid closure is similar to the closure in PDF methods,[40] except that molecular diffusion is also included exactly in LEMLES in addition to finite-rate kinetics $\dot{w}_k$. As in PDF methods, the large-scale transport is modeled as a Lagrangian transport of the scalar fields across LES cells, and the subgrid stirring is modeled. In PDF methods, a mixing model is often employed to model turbulent mixing, whereas, in LEMLES, small-scale turbulent stirring is implemented by the triplet mapping process.

Subgrid Scalar Transport

The transport of the subgrid scalar field, Eq. (23), is carried out across the LES cell faces in a Lagrangian manner. This transport is achieved using a "splicing" technique. Splicing involves the transfer of LEM cells between the LES control volumes accounting for the mass flux across each LES cell face. The mass flux on each of the six control surfaces (for hexahedral control volume) is first sorted in an ascending order following sign convention of positive influx and negative efflux. The number of LEM cells is then determined based on the amount of mass flux that needs to be transported across each LES cell face. At many locations, fractional LEM cells have to be transported to maintain mass conservation. Mass transported out of the LEM domain is taken out from one end of the one-dimensional domain and mass transport in is added to the other end of the one-dimensional domain. Further details are given elsewhere.[10,13,15]

Volumetric Expansion

Combustion at the subgrid level increases the temperature and decreases the local density (because pressure is assumed to be constant in the subgrid between LES time step). This effect results in a volumetric expansion and is included explicitly by expanding the LEM domain by an amount equal to

$$\Delta V^*_{\mathrm{LEM},i} = \rho_i^n \big/ \rho_i^* \tag{28}$$

where $\Delta V_{\mathrm{LEM},i}$ is the change in volume of LEM cell i. Here ρ_i^n and ρ_i^* are, respectively, the density of the ith cell at the previous and the current time-integration levels in the LEM simulation [not at the fluid-dynamic time step, $(\Delta t_{\mathrm{LES}})$ at LES level].

Because we have assumed that the length of the LEM one-dimensional domain is the grid size $\bar{\Delta}$ (an assumption that is not necessary but used here for computational expediency[10]), volumetric expansion will require regridding of the LEM domain to maintain the same length. In the present study, regridding is done after the large-scale advection process. Regridding does introduce some spurious diffusion when properties within some cells are redistributed. However, this is not a very serious issue because very few LEM cells are involved and because, overall, the amount of mass convected out and into a LES cell is approximately the same at every time step (because we enforce strict mass conservation).

Conservation of mass, momentum, and energy (at the LES level) and conservation of mass, energy, and species (at the LEM level) are fully coupled. Chemical reaction at the LEM level determines heat release and thermal expansion at the LEM level, which at the LES level generates flow motion that, in turns, transports the species field at the LEM level. Full coupling is maintained in the LEMLES to ensure local mass conservation.

Combustion Modeling

In this study, we have employed two liquid fuels: n-heptane and kerosene. In both cases, global reduced mechanisms are employed. For n-heptane, we employ a single-step, five-species model,[41] and for kerosene, we employ a three-step, seven-species global mechanism[42] of the form

$$\mathrm{C}_n\mathrm{H}_m + (n/2 + m/4)\mathrm{O}_2 \longrightarrow n\mathrm{CO} + (m/2)\mathrm{H}_2\mathrm{O} \tag{29}$$

$$2\mathrm{CO} + \mathrm{O}_2 \longrightarrow 2\mathrm{CO}_2 \tag{30}$$

$$\mathrm{N}_2 + \mathrm{O}_2 \longrightarrow 2\mathrm{NO} \tag{31}$$

with $n = 12$ and $m = 23$. For n-heptane–air combustion, we study global heat release and unburned hydrocarbons (UHC), here identified simply as unburned fuel, in the combustor. In the kerosene–air cases, we investigate not only global heat-release effects but also CO, NO, and UHC distribution in the combustor.

The closure for the reaction rate is particularly important because it strongly impacts the LES prediction. Two LES closures for $\bar{\dot{w}}_k$ are compared in this study: a conventional approach that employs a subgrid eddy breakup model (called EBULES, hereafter)[43] and LEMLES. In EBULES, the filtered reaction rate $\bar{\dot{w}}_k$ is obtained from the relation

$$\bar{\dot{w}}_k = 1/(1/\dot{w}_{\mathrm{mix}} + 1/\dot{w}_k) \tag{32}$$

where $\dot{w}_k$ is the chemical rate for a specific species and $\dot{w}_{\mathrm{mix}} \propto [X_k]/\tau_{\mathrm{mix}}$. Here $[X_k]$ is the concentration of the kth species, and τ_{mix} is the mixing time that is determined as $\tau_{\mathrm{mix}} \propto \bar{\Delta}/\sqrt{k^{\mathrm{sgs}}}$. The proportionality constant is chosen as unity[43] for these studies.

In LEMLES, no such closure is needed because the exact reaction kinetics are simulated exactly within each LES cell.

Liquid Phase

The dispersed phase is modeled using the Lagrangian model,[25] which solves for the individual droplet evolution in space and time within the gas field. However, to maintain computational expediency, a sampling technique is employed, whereby characteristic groups of droplets, all having identical size, location, velocity, and temperature, are represented as "computational parcels" and are then tracked using the Lagrangian approach.

A dilute spray formulation[25] is used in this study. It is well known that this approach is invalid in the near field of the injectors where the droplet collisions are high. However, the physical processes of interest, such as droplet dispersion, evaporation, fuel–air mixing, and combustion, that occur farther away from the injector (where the dilute spray approximation is valid) can be simulated using this model. Breakup models are currently being implemented to account for both primary and secondary breakup processes.

Coupling between the dispersed phase and the gas phase is by the interphase exchange source terms that appear on the right-hand side of the LES equations, for example, Eqs. (2). These terms are computed, as described elsewhere,[25] and therefore only briefly summarized next.

In modeling the spray field, it is assumed that the Kolmogorov scale is of the same order or larger than the largest droplet in the spray field. For such a situation, the interaction between gas and liquid phases is dominated by laminar fluid dynamics. The governing equations for the transport of dispersed phase are given by

$$\frac{\mathrm{d}x_{i,d}}{\mathrm{d}t} = u_{i,d} \tag{33}$$

$$\frac{\mathrm{d}m_d}{\mathrm{d}t} = -\dot{m}_d \tag{34}$$

$$\frac{\mathrm{d}u_{i,d}}{\mathrm{d}t} = \frac{3}{16}\frac{C_D \mu Re_d}{\rho_d r_d^2}(u_i - u_{i,d}) \tag{35}$$

$$m_d C_d \frac{\mathrm{d}T_d}{\mathrm{d}t} = h_d \pi d_d^2 (\tilde{T} - T_d) - \dot{m}_d L_v \tag{36}$$

Here all variables with subscript d indicated droplet properties, $u_{i,d}$ is the ith component of the droplet velocity, ρ_d is the droplet density, and d_d $(= 2r_d)$ is the diameter of the droplet. Re_d is the droplet

Reynolds number defined as $Re_d = \sqrt{[(u_i - u_{i,d})(u_i - u_{i,d})]}d_d/\nu$, where C_D is the drag coefficient obtained from empirical correlations for evaporating droplets (assuming that they retain the spherical shape). The mass of the particle is given by $m_d = (4/3)\pi r_d^3 \rho_d$, and $\dot{m}_d$ is the net mass transfer rate for a droplet in a convective flow field. In the preceding equations, C_d and L_v are, respectively, the specific heat for the droplet and latent heat for vaporization. The heat-transfer coefficient h_d for a droplet in a convective flowfield with mass transfer is modeled using the correlation proposed earlier.[25]

Ignoring the effect of subgrid turbulence on the droplet motion is not realistic because the droplets are limited to deterministic trajectories prescribed by their initial condition and mean gas properties. Here, the effect of turbulence on the droplet motion is simulated using the stochastic-separated-flow (SSF) model.[25] The stochastic dispersion of droplets caused by turbulent motion is incorporated by representing the gas-phase velocity at particle location as $u_i = \tilde{u}_i + X\sqrt{(2k^{\text{sgs}}/3)}$, where X is a random number, sampled from a uniform distribution (with zero mean). The LDKM model's prediction of k^{sgs} provides the necessary information to include this stochastic dispersion in the current LES.

Because particles are not restricted to lie on the Eulerian grid points where the gas-phase properties are known, a volume-weighted interpolation is used to estimate the gas-phase properties at the droplet locations, as well as, for the redistribution of the spray source terms from the particle position to the Eulerian grid (gas phase). The accuracy of this interpolation is maintained as either second or fourth order to be consistent with the overall accuracy of the numerical scheme.

Liquid-Gas Coupling

Coupling between the dispersed phase and the gas phase are provided by the interphase exchange terms or the source terms that appear on the right-hand side of the LES equations. These are computed as follows[21,25]:

$$\begin{pmatrix} \dot{\rho}_s \\ \dot{F}_{s,i} \\ \dot{Q}_s \\ \dot{S}_{s,k} \end{pmatrix} = -\begin{pmatrix} \dfrac{\mathrm{d}m_d}{\mathrm{d}t} \\ \dfrac{\mathrm{d}m_d u_i}{\mathrm{d}t} \\ \dfrac{\mathrm{d}m_d e_d}{\mathrm{d}t} \\ \dfrac{\mathrm{d}m_d Y_k}{\mathrm{d}t} \end{pmatrix} = -\begin{pmatrix} \rho_d \dfrac{\mathrm{d}V_d}{\mathrm{d}t} + V_d \dfrac{\mathrm{d}\rho_d}{\mathrm{d}t} \\ m_d \dfrac{\mathrm{d}u_{i,d}}{\mathrm{d}t} + u_{i,d} \dfrac{\mathrm{d}m_d}{\mathrm{d}t} \\ m_d \dfrac{\mathrm{d}e_d}{\mathrm{d}t} + e_d \dfrac{\mathrm{d}m_d}{\mathrm{d}t} \\ m_d \dfrac{\mathrm{d}Y_{k,d}}{\mathrm{d}t} + Y_{k,d} \dfrac{\mathrm{d}m_d}{\mathrm{d}t} \end{pmatrix}$$

Here ρ_d, V_d, $u_{i,d}$, e_d, and $Y_{k,d}$ are the density, volume, ith component of the velocity, total energy, and species mass fraction of the fuel in the droplets, respectively.

In the preceding equations, the droplet mass is $m_d = \rho_d V_d$, the droplet volume is $V_d = 4\pi r_d^3/3$, the droplet internal energy is $e_d = C_L T_d$, where C_L is the liquid heat capacity, and the droplet evaporation rate is $\mathrm{d}m_d/\mathrm{d}t = -\dot{m}_d$. Further, simplifications can be made by realizing that only single component fuels are considered in this study. This implies that the mass fraction of fuel species in the liquid droplet is always unity, that is, $Y_{k,d} = 1$ and $\mathrm{d}Y_{k,d}/\mathrm{d}t = 0$.

The final source terms for a single droplet can be summarized as[25]

$$\begin{pmatrix} \dot{\rho}_s \\ \dot{F}_{s,i} \\ \dot{Q}_s \\ \dot{S}_{s,k} \end{pmatrix} = \begin{pmatrix} \dot{m}_d \\ \dot{m}_d u_{i,d} - \dfrac{4\pi}{3}\rho_d r_d^2 \dfrac{\mathrm{d}u_{i,d}}{\mathrm{d}t} \\ \dot{m}_d h_{v,s} - h_d \pi d_d^2 (\tilde{T} - T_d) \\ \dot{m}_d \end{pmatrix}$$

The preceding relations are for a single droplet moving in a flowfield. To track groups of particles (computational parcels), rather than individual particles, the interphase exchange terms needs to be multiplied by the number of particles present per group for mass conservation. This approach, besides allowing for a statistically significant number of particles to be tracked, also helps to control the mass flow rate of the liquid.

Thus, if n_d number of particles are present per group, then the volume-averaged source terms for all of the droplet group trajectories that cross a computational cell are computed by summing the contribution from every group as follows:

$$\begin{pmatrix} \widetilde{\dot{\rho}_s} \\ \widetilde{\dot{F}_{s,i}} \\ \widetilde{\dot{Q}_s} \\ \widetilde{\dot{S}_{s,k}} \end{pmatrix} = \begin{pmatrix} \displaystyle\sum_m n_d \dot{m}_d \\ \displaystyle\sum_m n_d \left[\dot{m}_d u_{i,d} - \frac{4\pi}{3}\rho_d r_d^2 \frac{\mathrm{d}u_{i,d}}{\mathrm{d}t} \right] \\ \displaystyle\sum_m n_d \left[\dot{m}_d h_{v,s} - h_d \pi d_d^2 (\tilde{T} - T_d) \right] \\ \displaystyle\sum_m n_d \dot{m}_d \end{pmatrix}$$

where the summation index m is over all of the droplet groups crossing a computational cell volume. These terms are used to couple to the LES gas-phase equations. Additional details are given in the cited literature.

Numerical Implementation

The LES solver has been extensively validated for many gas turbine applications (see references just cited) and is a finite volume scheme that is nominally second-order accurate in space and time. There is an option to switch to fourth-order spatial accuracy for acquiring final statistics.

Test Cases

We discuss two liquid-fueled combustors in this paper, identified as GE-1 and GE-2. GE-1 is a laboratory-scale combustor that is currently being used at Georgia Tech to study LBO. It employs a full-scale General Electric CFM56 premixer in the inlet, but the combustor section is designed to operate at atmospheric conditions. Preheated air at 379 K enters this combustor in a swirling manner, and fuel (Jet A or kerosene) is injected from the central spray injector. Detailed measurements (for reacting case) using laser Doppler velocimetry (LDV) and phase Doppler particle analyzer (PDPA) are ongoing[44] to obtain data for LES model validation. We report here our model validation for the nonreacting swirling case. Comparison of LES prediction with data for the reacting case will be reported elsewhere.

Figure 1 shows schematically this combustor, along with the grid distribution. The combustor length from the dump plane to the exit is 0.278 m, the height is 0.0896 m, and the width is 0.0737 m (lower) and 0.103 m (upper). The circular inlet diameter at the dump plane is 0.04026 m, and the actual inlet is approximately 0.0152 mm upstream of the dump plane. This upstream location is just downstream of the actual inlet premixer swirl vanes. The swirl vanes and the internal details have not been modeled in the current study,

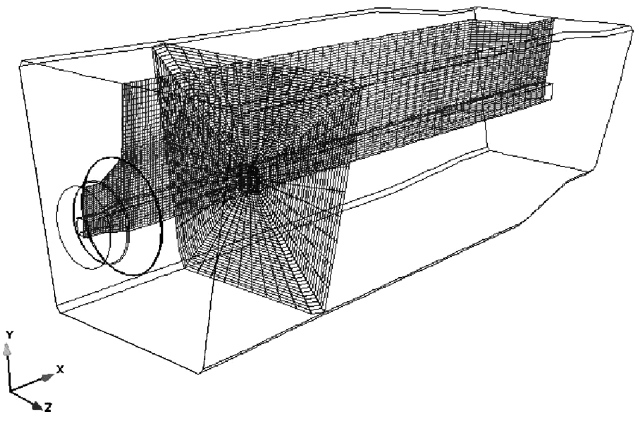

Fig. 1 Schematic of the GE-1 combustor.

and, therefore, the inflow velocity profiles at the computational inlet are considered approximate. An effort is currently underway that employs a generalized multiblock LES solver to fully resolve the internal features in the inlet. These results will be reported in the near future.

We employ a two-domain, butterfly grid to resolve the central core of the combustor using a Cartesian grid while a body-conforming grid is employed elsewhere. Various grid resolutions were used initially to investigate grid quality. For all results reported here, a grid of $185 \times 74 \times 81$ is employed for the outer body-conforming grid and a grid of $185 \times 21 \times 21$ is employed in the central Cartesian grid. The grid stretching is less than 5% in the near field, and stretching increases to a maximum of around 8% axially only near the outflow. The minimum resolution in the inlet shear layer region is around 0.3 mm in the axial direction, 0.26 mm in the radial direction, and 0.25 mm in the azimuthal direction. With this resolution, nearly 16 points are in the shear layer width, which is considered adequate.

The second combustor, GE-2, is a full-scale sector consisting of two cups operating under realistic conditions[45] and consists of multiple annular swirlers that surround the primary injector. Two operating conditions are studied here: case 1, pilot only (startup); and case 2, pilot and main (full power). Case 1 operates at around 9 atm with preheated air at around 580 K. Fuel flow rate is equally distributed between the two cups. For case 2, the combustor operates at around 24 atm with preheated air at around 900 K. Fuel is injected from the primary injector and from 20 injectors placed equally apart on the rim surrounding the primary cups. Again, total fuel flow rate is split equally between the two cups.

Figures 2a and 2b show this configuration from two perspectives. Note that although the two cups are identical, the sector shapes are not. Therefore, the regions downstream of the two cups are not the same, and significant three-dimensional interaction between the two cups occurs, as is discussed later. The length of the modeled combustor is approximately 0.159 m, width is 0.067 m, and height is around 0.173 m. Because of the complexity of this geometry, an embedded boundary method[46] is used to resolve the geometry in the inlet. As in GE-1 case, the inlet region is approximated from downstream of the premixer, and some of the inlet details are not modeled. The resolution is around 0.3 mm in all directions, and near the inlet the swirling shear layers are well resolved, with around 20 points in the shear region. A total of around 6.9 million grid points ($178 \times 258 \times 148$) are used to resolve the flowfield. For LEMLES, we resolve the subgrid structure within each LES cell by 12 LEM cells.

For the nominal conditions just noted, the Reynolds number (based on the inlet diameter, $D_0 = 2R_0$ at the dump plane, and an inlet bulk velocity U_0), $Re_D = U_0 D_0/\nu$ is 76.98×10^3 ($D_0 = 0.0426$ m and $U_0 = 46$ m/s) for the GE-1 combustor, and 2.2×10^6 ($D_0 = 0.14$ m and $U_0 = 100$ m/s) for the GE-2 (case 2). At the dump plane, using the computed k^{sgs} to estimate the subgrid velocity fluctuation u', and an integral length scale $l \approx 0.65 D_0$, the turbulence Reynolds number $Re_l = u' l/\nu$ is estimated around 19.5×10^3 and 16.4×10^4 for GE-1 and GE-2 (case 2), respectively. The corresponding subgrid Reynolds number $Re_{\bar{\Delta}} = u' \bar{\Delta}/\nu$ is 173 for GE-1 and around 420 for GE-2 (case 2). Using scaling relations, the Kolmogorov scale η is 0.0183 and 0.013 mm, respectively, for the two combustors in the high turbulence region.

Note that these are just order-of-magnitude estimates because some of the characteristics scales are difficult to define exactly (e.g., inlet D_0 for GE-2 might not be the proper reference scale because of the complexity of the design, and axial velocity changes rapidly as it approaches the dump plane). However, the extremely high values of Re_D, Re_l, and $Re_{\bar{\Delta}}$ for GE-2 (case 2) are partly caused by the high pressure (and, hence, high density) of the inlet air at the inlet. Downstream of the dump plane, the flow rapidly slows down (see discussion later), and k^{sgs} decreases rapidly as a result of the formation of the VBB and combustion heat release (which increases viscosity). These effects combine to reduce the local Reynolds number considerably. Analysis of the local values of $Re_{\bar{\Delta}}$ suggests that, in general, subgrid resolution used in LEMLES resolves around $1–5\eta$ in the regions of interest. Thus, the current resolution used for LEMLES is considered quite adequate.

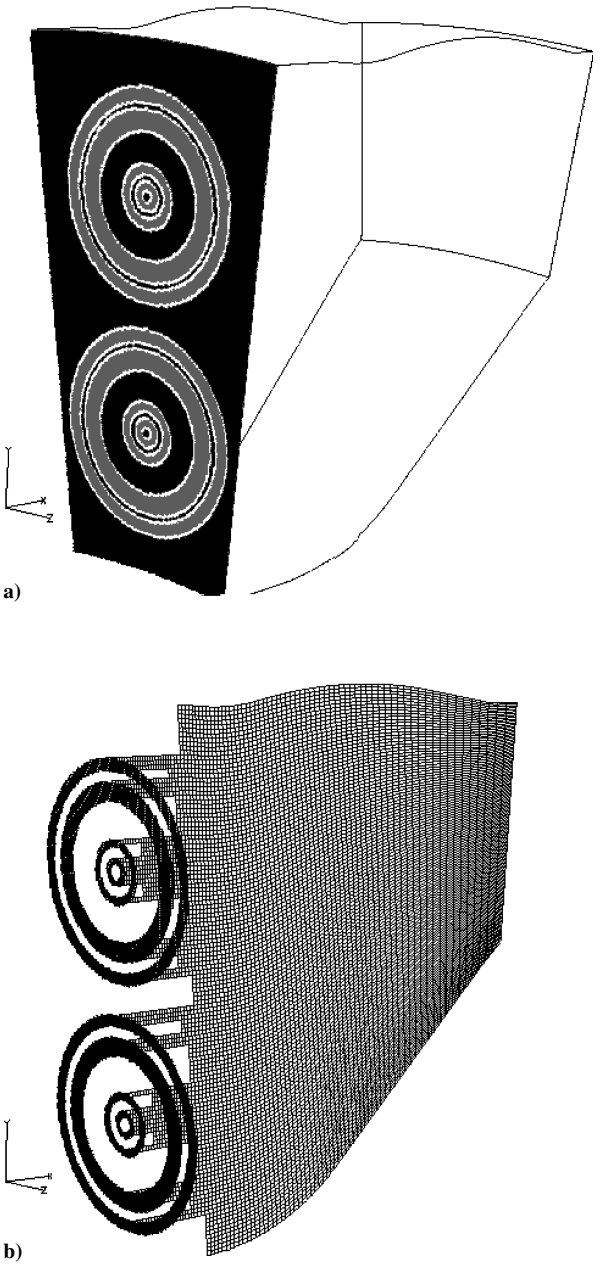

Fig. 2 Schematic of the GE-2 combustor.

Spray is injected using the SSF approach using parcels to represent groups of droplets with similar properties. Typically, around 150,000–350,000 droplet parcels (with 5–10 particles per group) are present (the higher value corresponds to case 2), on an average. A log-normal distribution with a Sauter mean diameter of 20 μm is used for case 1 and 15 μm for case 2, with a droplet cutoff radius of 2 μm.

Inflow Conditions

Inflow initialization for both combustors is a major issue for LES. Ideally, simulation should include the upstream premixer and solve for the flow through the swirl vanes. This is an approach that is currently being tested and will be demonstrated in the near future. Here, we approximate the inflow profiles just downstream of the premixer (but inside the inlet) based on past experience.[47]

Figures 3a and 3b show, respectively, the inflow velocity profiles employed in GE-1 and GE-2. For the GE-2 case, profiles in the secondary annular outer regions are specified as fully developed pipe flow. A 7% inflow turbulence field is also included in the primary swirl cup flow, and a similar initialization is used for the subgrid kinetic energy k^{sgs}.

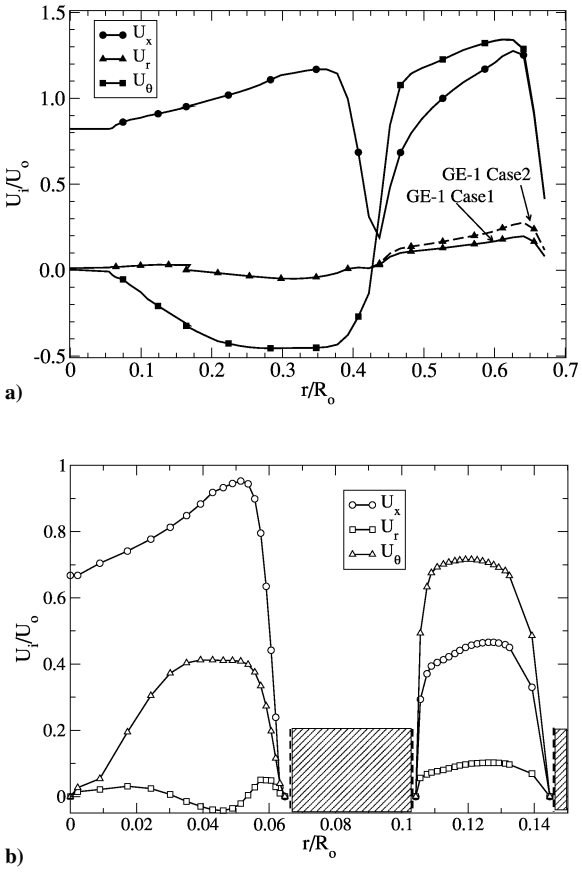

Fig. 3 Inflow profiles used for the two combustors.

Time-Step Restriction for Two-Phase Flow

There are many time steps of importance in this type of problem. In addition to the usual LES time step (Δt_{LES}), subgrid processes in LEMLES have additional time steps for 1) reaction-diffusion Δt_{LEM}, 2) subgrid stirring Δt_{stir}, and 3) large-scale advection Δt_{sp}. The LES time step Δt_{LES} is the explicit time step determined by stability consideration. To maintain strict mass conservation, $\Delta t_{\text{sp}} = \Delta t_{\text{LES}}$. Δt_{stir} is determined from the stirring frequency λ [Eq. (26)], and Δt_{LEM} is determined by the minimum of the chemical and diffusion time within each cell needed for stable integration of the LEM equation (25).

Inclusion of spray introduces more timescales in the flow. To accurately calculate the particle trajectories, size and temperature, the Lagrangian time step used for the integration has to be the smallest of the various physical timescales. The various timescales are 1) Δt_{LES}, 2) the droplet velocity relaxation time, 3) the droplet life time, 4) the turbulent eddy droplet interaction time, and 5) the droplet surface temperature constraint time. At any instant, the smallest of the timescales is used for particle evolution.[25]

Computational Issues

Simulations are carried out using a parallel solver on an in-house 128-processor Intel PC Linux cluster with dual Pentium Xeon processors operating at 2.2 GHz and using an Infiniband switched network. The solver is not optimized for this cluster as yet, and furthermore, parallel optimization for spray modeling, including proper load balancing, is still an issue of research. All simulations were carried out long enough to collect statistics. Typically, three flow-through times are used for statistical analysis, after the initial transients are neglected.

Typical cost for a single flow-through time for the nonreacting GE-1 case is around 1200 single processor hours. For EBULES of the GE-2 combustor, the cost is around 3200 single processor hours, whereas for LEMLES (for GE-2, case 2) it is factor of seven higher. Past studies[3] have shown that the inclusion of species (without chemical kinetics) in LEMLES increases the overall cost by only 20% more than EBULES. Therefore, the computational cost primarily increases as a result of finite-rate kinetics employed in this study. The overall turnaround time for LEMLES can be reduced by increasing the number of processors and by further optimization of the code. Past studies[3,17] have shown that the cost for finite-rate kinetics can be reduced by a factor 10–15 (depending on the kinetics mechanism) by using ISAT.[38]

Results and Discussion

We first discuss the comparison of the current LES with cold-flow measurements in the GE-1 combustor and then focus on the physics of combustion in the GE-2.

Nonreacting Flow in GE-1

Measurements for nonreacting cold flow have been obtained using LDV. Two velocity components in coincidence mode have been obtained at various axial locations in the horizontal and vertical center planes. Details of these measurements will be reported soon.[44] Because the inflow conditions for LES in the inlet have been approximated in the current study, a series of simulations were initially conducted (not shown here, for brevity) to determine the sensitivity of the predictions to the inflow profiles. It was determined that once the bulk flow and swirl conditions are satisfied by the axial and azimuthal velocity, small variations in the radial profiles (see cases 1 and 2 for GE-1 in Fig. 3a) can impact the near field, but the far-field variation is relatively insensitive.

This is demonstrated in Fig. 4, which shows the centerline mean axial-velocity profile (normalized by the inlet bulk velocity U_0) for the baseline case (GE-1, case 1) and for another case (GE-1, case 2), which uses a slightly different radial profile (Fig. 3a). It can be seen that although the beginning of the VBB is changed by this (very slight) inflow radial profile adjustment, the peak negative velocity in the VBB, the extent of the VBB, and the final rate of increase in the axial velocity toward the outflow are less sensitive to this change. At the centerline, the length of the VBB is around $x/R_0 = 7$, with peak negative axial velocity of around $0.25U_0$ in the VBB. It is also clear in both the measurements and in the LES, that the upstream location of the VBB is actually located inside the inlet. The predicted variation in the region $(0 < x/R_0 < 1)$ is substantially different than the measured values, and this might be caused by the uncertainty in the inflow geometry. Nevertheless, subsequent evolution is well reproduced, which suggests that the overal mass flux and flow conditions are modeled accurately.

Figures 5a and 5b show the normalized mean axial-velocity profiles in the combustor at various axial locations. Two center planes are shown: a horizontal x–z plane (Fig. 5a) and a vertical x–y plane (Fig. 5b). The experimental data obtained at some of the axial locations are also shown. It can be seen that at the first location where data are available for comparison the peak value in the reverse flow region is underpredicted by the LES and is consistent with the

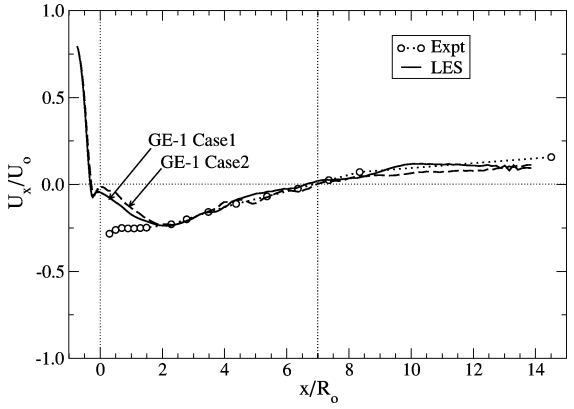

Fig. 4 Comparison of predicted centerline variation of mean axial velocity with data.

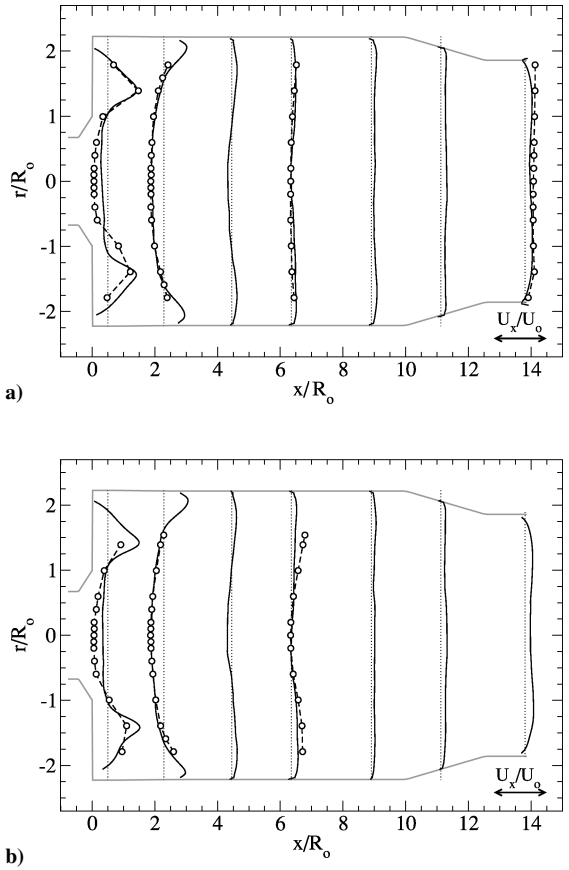

Fig. 5 Comparison of predicted mean axial-velocity profiles with data along two center planes.

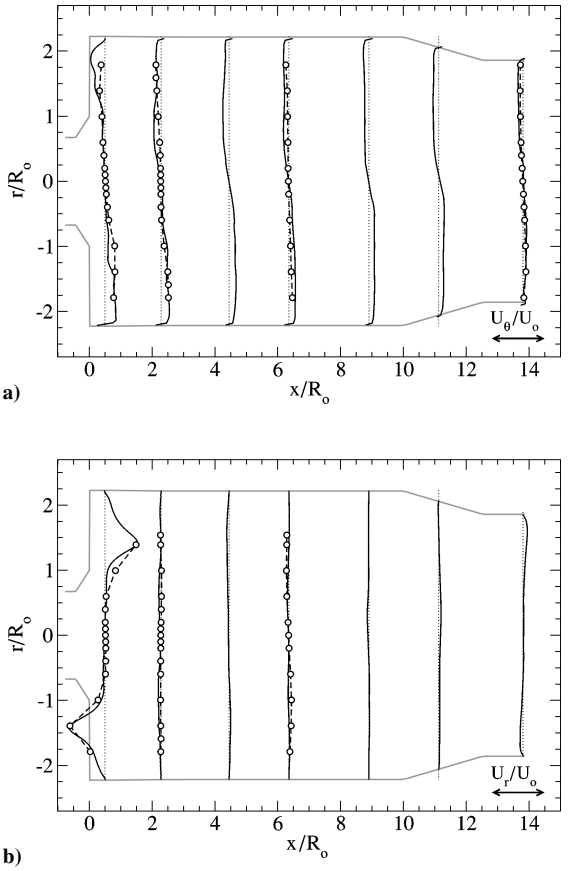

Fig. 6 Comparison of predicted mean normal velocity profiles with data along two center planes.

underprediction of the centerline profile shown earlier. The peak value in the shear-layer region is well predicted and so is the peak location. Further downstream, the dynamics in the combustor takes over, with the formation of the VBB (see discussion later). As a result, the comparison with measurements at all downstream locations is in very good agreement.

Figures 6a and 6b show, respectively, the normalized mean tangential velocity profiles in the x–z horizontal center plane and the radial velocity profiles in the x–y vertical center plane at various axial locations. For these normal components, both the peak magnitude as well as peak locations are well predicted. Further downstream the agreement remains quite good at all measured locations.

Comparisons for turbulence properties such as the streamwise $[\sqrt{(\overline{u_x u_x})}]$, the radial $[\sqrt{(\overline{u_r u_r})}]$, and the tangential $[\sqrt{(\overline{u_\theta u_\theta})}]$ rms velocity fluctuations are presented in Figs. 7 and 8. The profiles are normalized by $u'_0 = 20$ m/s, which represents the peak value seen in the axial rms profiles. There is some discrepancy between the prediction and data at the first measurement location near the edges (Fig. 7a). The experimental data show some asymmetry in the u_{RMS} profile for both the center planes at the first measurement location. The computational simulations predict the peak locations well in both cases; however, there is an underprediction in magnitude. This can be related to lack of realistic turbulence in the inlet. In the recirculation zone region, the turbulence properties agree well with data.

Figures 8a and 8b show, respectively, the tangential velocity fluctuation intensity profile in the x–z plane and the radial velocity fluctuation intensity profile in the x–y plane. The predicted profiles follow the measurements well at all axial locations. All fluctuating components decay and eventually approach uniform radial profile further downstream.

Overall, these comparison show the general ability of the LES approach used in this study. Comparison with the reacting data will be reported in the near future.

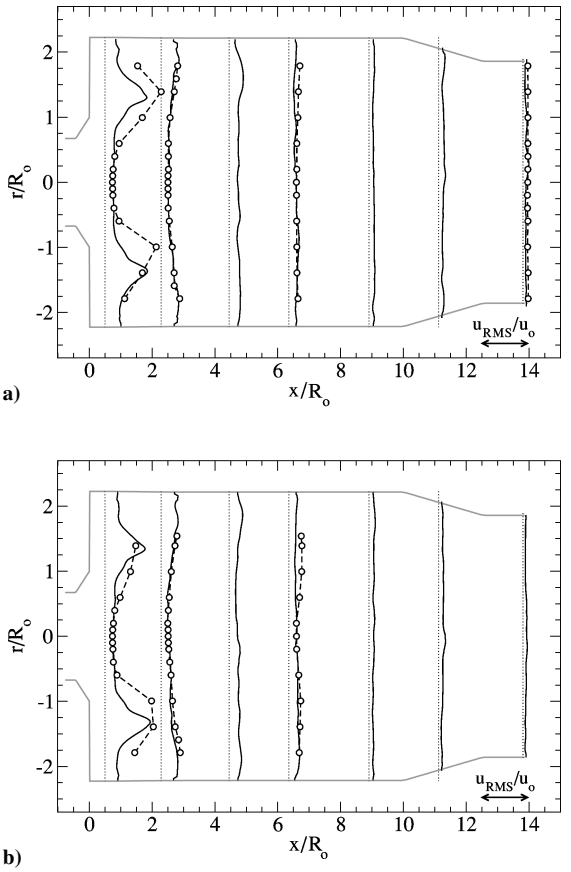

Fig. 7 Comparison of predicted rms axial-velocity profiles with data along two center planes.

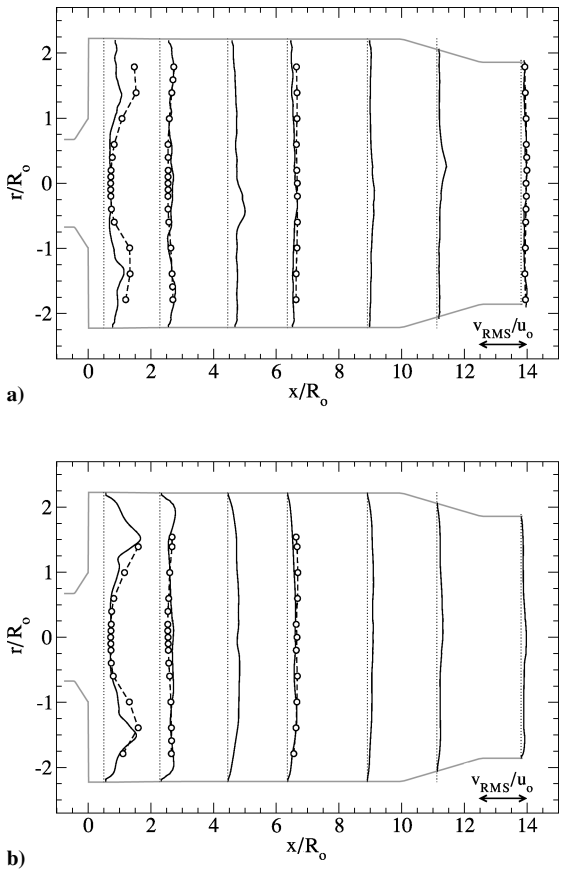

Fig. 8 Comparison of predicted rms normal velocity profiles with data along two center planes.

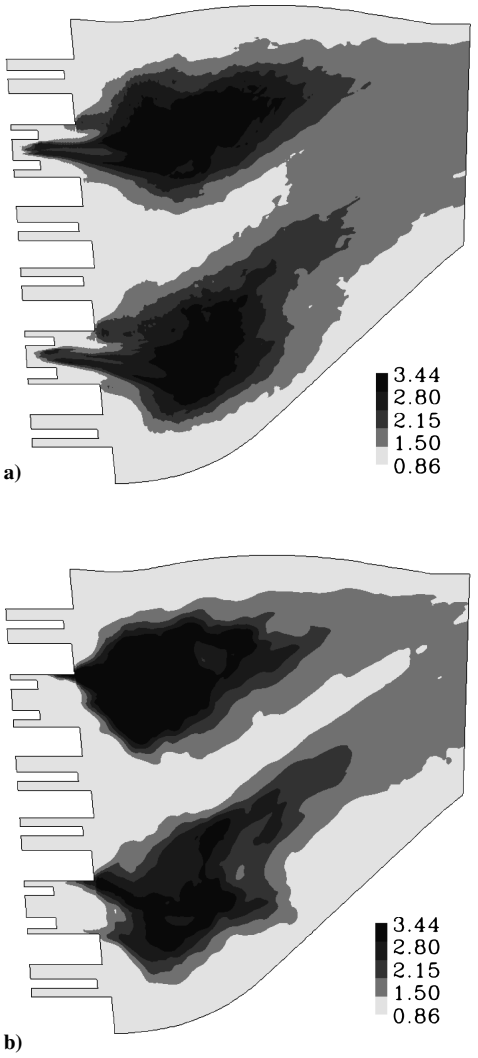

Fig. 9 Mean temperature contours in the *x–y* center plane for case 1, GE-2.

GE-2 Case 1

In this section, we discuss the GE-2 case 1 in which only the primary injector in the center of each cup is operating. This corresponds to a typical startup of this engine. We compare EBULES and LEMLES predictions for identical test conditions using the n-heptane spray model.

Figures 9a and 9b show, respectively, the EBULES and LEMLES prediction of the mean temperature in the center $x-y$ plane. Unless otherwise noted, all temperature fields are shown normalized by the inlet air temperature. Furthermore, the same contour interval (in gray-scale shading) is employed for direct comparison. Three key observations can be made from these figures. First, both cups operate individually, and the temperature fields only merge near the outflow. Second, because of the shape of the combustor, the flow features and temperature fields are quite different between the two cups. The region of high temperature is much larger and more uniform for the upper cup in both EBULES and LEMLES. This clearly demonstrates that the flow in these sectors is highly three dimensional even though the premixer, cup geometries, and the injection conditions in both the cups are identical. Third, EBULES predicts that the flame anchors inside the primary cup and immediately downstream of the injector. This is unphysical and is not observed in the real device. The EBULES has no in-built mechanisms to account for proper fuel–air molecular mixing time delay and for the resulting ignition delay. Therefore, EBULES ignites the mixture as soon as the fuel evaporates. This results in the unphysical positioning of the flame anchor in the inlet. Note that this effect is a limitation of the EBU closure and not an issue of lack of grid resolution.

On the other hand, in LEMLES fuel–air mixing has to occur properly before finite-rate kinetics can occur. As a result, the ignition of the mixture is delayed until it gets closer to the dump plane. Thus, in LEMLES the flame anchors at the dump plane and at a location that is qualitatively in good agreement with experimental observation in test rigs.

This ability of LEMLES to properly locate the spray flame without requiring any ad hoc model adjustment provides confidence in this approach's ability to deal with complex flame structures. This ability will be critical in the future when LES studies of LBO are conducted.

Figures 10a and 10b show, respectively, the time-averaged temperature profiles at the exit $y-z$ plane of the combustor for EBULES and LEMLES, respectively. The temperature at the exit is significantly lower than the peak value in the combustor and is more uniform, although there are some local hot spots. The field is diagonally aligned, which is caused by the combination of the clockwise swirl and the larger area in the upper half of the combustor. Although EBULES and LEMLES show similar features (e.g., the peak temperature region is more distinct in the upper cup), the latter approach shows the imprint of both cups more clearly.

For turbine design purposes, the time-averaged profiles at the combustor exit for temperature (often called "pattern factor") are needed. Additionally, the exit-plane profiles for the pollutants and other species are also of interest. Figures 11a and 11b show, respectively, the time-averaged exit-plane profiles of the mean temperature and the unburned fuel species mass fraction. The center-plane and the entire span-averaged profiles are shown for both EBULES and LEMLES in these figures. There is a substantial variation in the profile in the radial direction because the two cups are operating under slightly different conditions, as noted earlier. There is still some unburned fuel at the exit, but the level is quite low. Although the span-averaged profiles are radially uniform, there is substantial spanwise variation in the temperature field and in the UHC distribution that is not directly apparent in the span-averaged data.

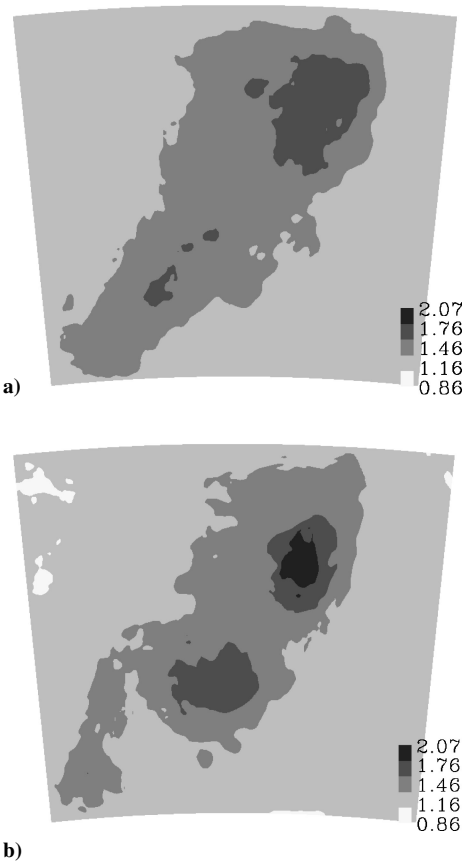

Fig. 10 Mean temperature contours at the exit y–z plane for case 1, GE-2.

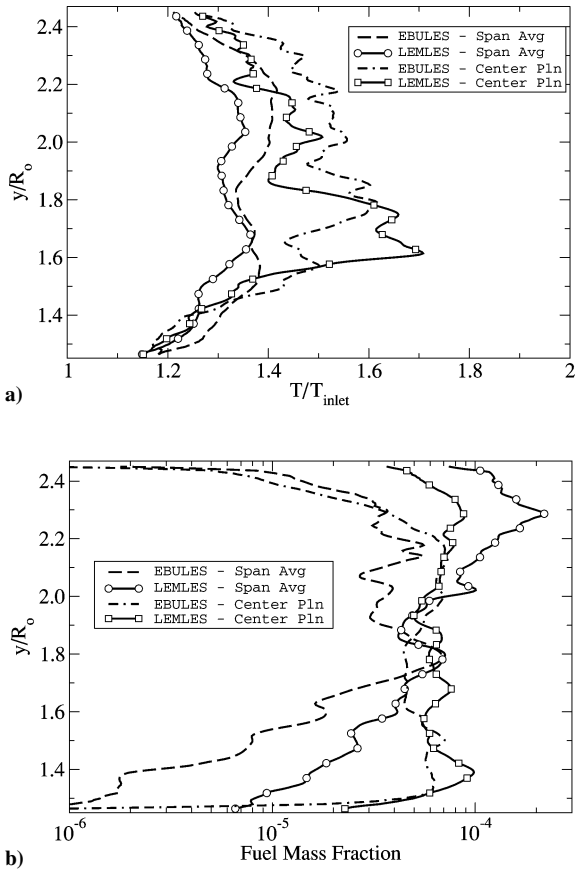

Fig. 11 Mean temperature and unburned fuel profiles at the exit for case 1, GE-2.

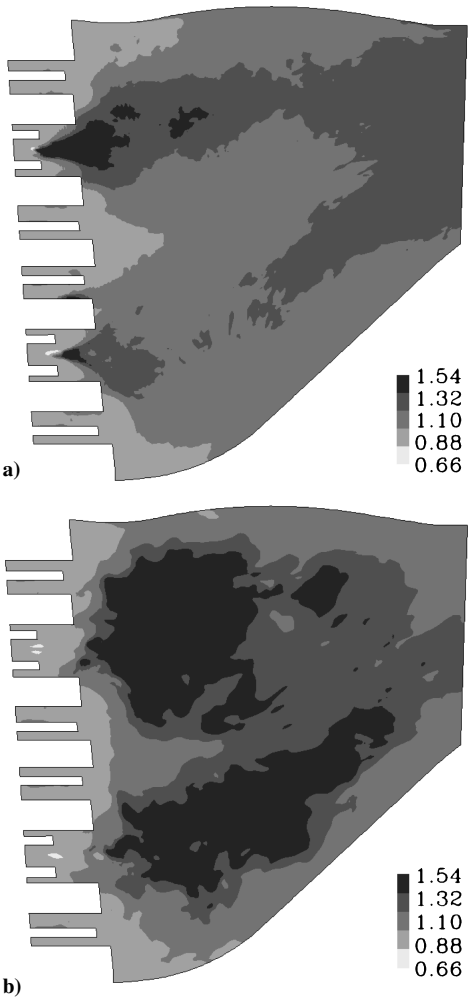

Fig. 12 Mean temperature contours in the center plane for case 2, GE-2.

GE-2 Case 2

The second case investigated is a full-power case in which fuel spray is injected from both the pilot injector in the center of the cup (used for case 1) and from the circular annular rim. For this study, we employ kerosene–air kinetics with a three-step model.

Figures 12a and 12b show, respectively, the normalized mean temperature in the center x–y plane for EBULES and LEMLES. There are some substantial differences between the EBULES and LEMLES results. The combustion process seems to be more complete in the LEMLES case with peak value of temperature uniform over a wide region in the combustor. In contrast, for EBULES most of the burning seems to be in the inlet, but there is still some combustion occurring even further downstream. Unlike case 1, the combustion region from the two cups merges relatively quickly around $x/R_0 = 2$. This is because fuel is injected from multiple locations (both from the primary injector and the 20 annular injectors), and this enables fuel–air mixing to occur more uniformly. The combustion region is still highly three-dimensional. EBULES again shows the anomalous anchoring of the flame inside the primary cup, and, in addition, the flame is also anchored on the outer rims as a result of secondary fuel injection. LEMLES, on the other hand, shows that the flame anchors along the walls of the dump plane, as in case 1.

Comparison of the LEMLES results for both cases shows that the flame structure is partially "lifted." Analysis shows that very close to the primary injectors the local strain rate is very high, and mixing between the vaporized fuel and air is not fully complete. In LEMLES, fuel–air mixing is explictly included in the subgrid, and, therefore, mixing delays are naturally reproduced. However, further downstream, the strain effects drop off rather quickly, and ignition of mixed fuel–air mixture takes place. It is also observed that the flame is consistently lifted away from the dump plane only

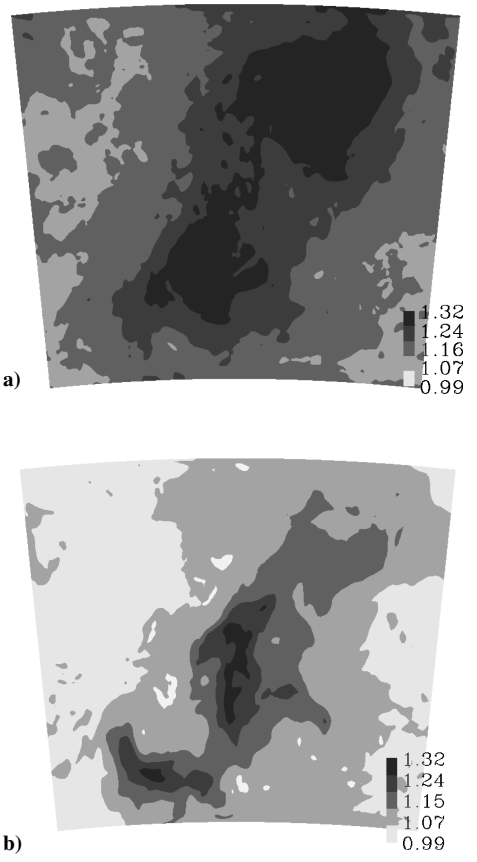

Fig. 13 Mean temperature contours at the exit for case 2.

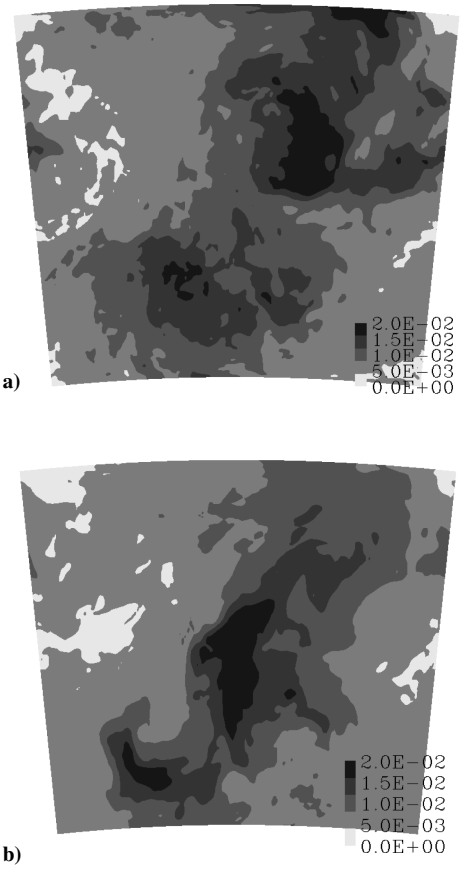

Fig. 14 Mean CO contours at the exit for case 2, GE-2.

for the lower cup. The shape of the combustor, which pushes the flow upward from the lower cup region, might be contributing partly to this effect.

Figures 13a and 13b show, respectively, the EBULES and LEMLES prediction of the mean temperature at the outflow plane. Again, there are substantial differences between the two simulation approaches. The EBULES shows regions of high peak values compared to LEMLES. This is because, in the latter case, fuel is consumed more efficiently further upstream and the outflow is more uniform. Figures 14a and 14b show, respectively, the corresponding exit plane contours of the mean CO mass fraction for the two cases. Because of the higher peak temperature near the outflow in the EBULES case, there are more regions with high values of CO concentration at the outflow, when compared to LEMLES. Thus, it is clear that combustion is more incomplete in the former case. This might be a limitation of the subgrid EBU closure because downstream of the dump plane k^{sgs} drops rapidly, and the mixing time estimate might not be correct.

The time-averaged, span-averaged, and center-plane profiles at the exit plane for temperature, CO, NO, and CO_2, are shown in Figs. 15a and 15b for EBULES and LEMLES, respectively. It can be seen that the span-averaged profiles show a relatively smoother radial variation. Note that this radial profile is much more smooth when compared to the case 1. However, there is still substantial local variation, as can be seen from the center-plane radial profiles. In general, both methods predict similar order of magnitude of CO and NO levels, although the radial variations and the actual numbers are different. Comparison with measurements are planned in the near future to evaluate the overall accuracy of these simulations.

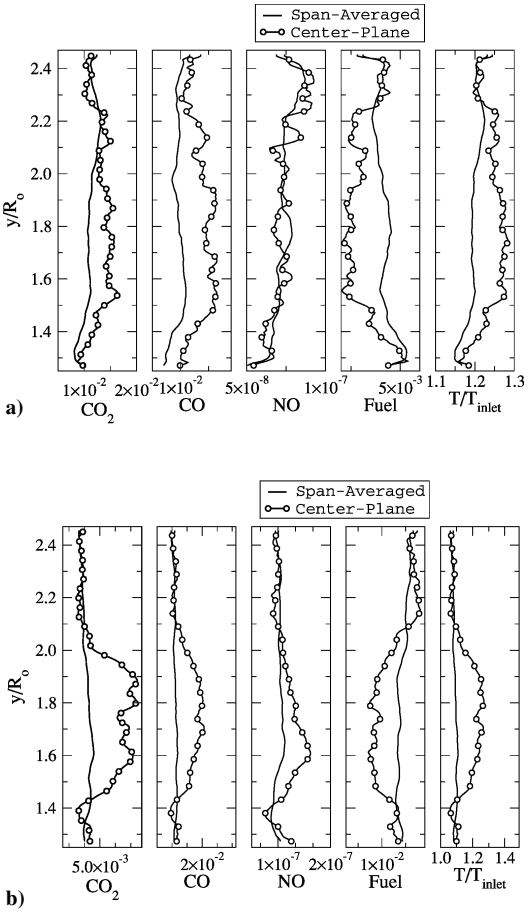

Fig. 15 Mean temperature, CO_2, CO, NO, and UHC profiles at the exit plane for case 2, GE-2.

Unsteady Features in the Combustor

In the following, we discuss some of the unsteady features seen in these simulations. Figure 16 show the streamlines and VBB region for the GE-1 combustor. It can be seen that the bubble is a single contiguous region and the flow swirls into and around the VBB. The swirl effect weakens near the outflow, and the flow is primarily axial by the time the outflow is reached. Analysis of the time evolution

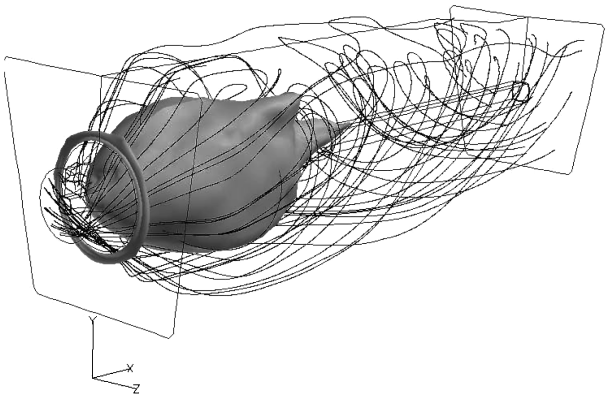

Fig. 16 Streamlines and vortex breakdown bubble in GE-1.

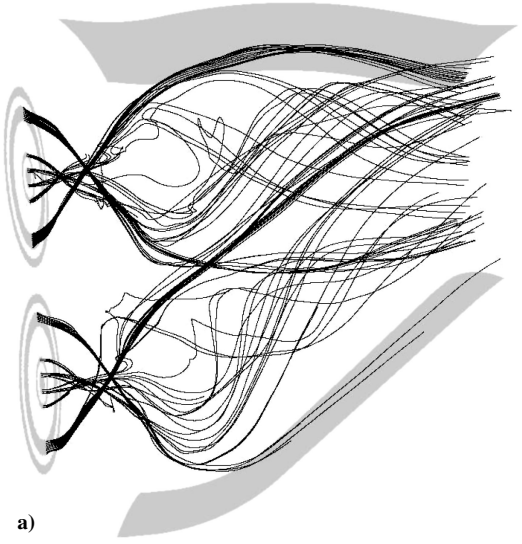

a)

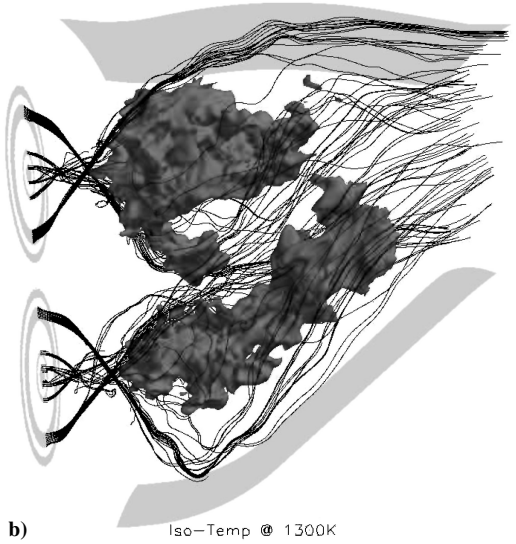

b)

Fig. 17 Streamline pattern at the center plane in GE-2.

of the solution shows that the VBB is not stationary and oscillates in the axial direction with a small lateral movement.

Because EBULES and LEMLES results are qualitatively similar, we discuss only the LEMLES results for GE-2. Figures 17a and 17b show the streamlines for the GE-2, cases 1 and 2, respectively. In both cases, it can be seen that the swirl flow from both cups interacts strongly downstream of the dump plane. For case 2, we also show isocontours of the temperature at an arbitrarily chosen value of 1300 K. It can be seen that the flame structure is longer and lifted up for the lower cup with the entire burning region "trapped"

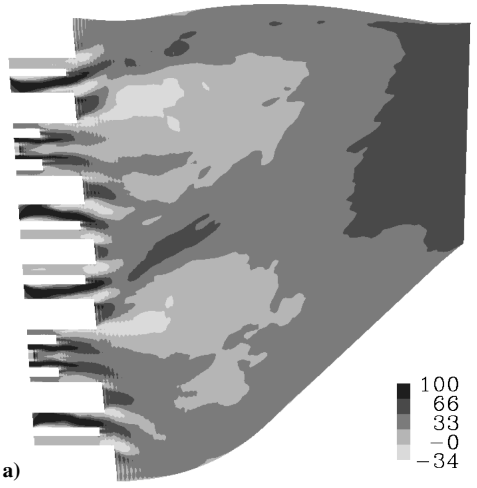

a)

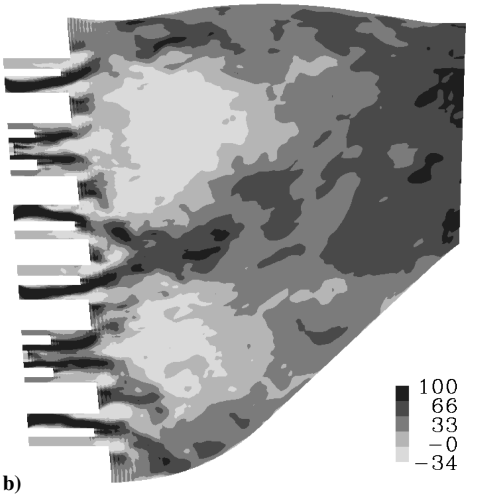

b)

Fig. 18 Mean axial-velocity contours at the center plane in GE-2.

between the outer periphery of the swirling flow. The streamlines for the lower cup seem to bounce off the bottom wall and penetrate into the flow from the upper cup. Instantaneous flow visualization shows that the three-dimensional effect is quite significant because of the shape of the combustor. Lower wall accelerates the flow both axially and transversely. Observation of the time evolution of the flow also shows that the secondary airflow from the outer rims of the primary is rotating approximately twice before reaching the outflow. The flow from the primary cup is entrained into the VBB regions and also transported outward to interact with the outer swirling flow. Strong mixing between the flow from the two cups is evident halfway into the combustor.

Further analysis shows that the GE-2 case has multiple regions of recirculation because of the geometrical design of this combustor, in addition to the primary VBB. The presence of multiple recirculation regions or VBBs in the GE-2 can be seen in Figs. 18a and 18b, which show, respectively, the axial-velocity contours for cases 1 and 2, respectively. Regions of negative velocity (the lightest shades) indicate reverse flow and the presence of recirculation. There is a large region of VBB primarily downstream of the upper-cup dump plane. However, the VBB for the lower cup is less distinct and is pushed upward as a result of the increased upward acceleration of the flow caused by the shape of the lower wall. The case 2 VBBs are more distinct and larger when compared to case 1. Thus, the VBB stabilizing mechanism is dominant for the full power case.

Very close to the dump plane, additional smaller regions of recirculation can be clearly seen adjacent to the lip of the inlet walls. It appears that these multiple regions of recirculation around the periphery of the primary cup might also be anchoring the spray flame. The larger VBBs that exist downstream of the dump plane clearly provide a stronger stabilizing mechanism to hold the spray field in

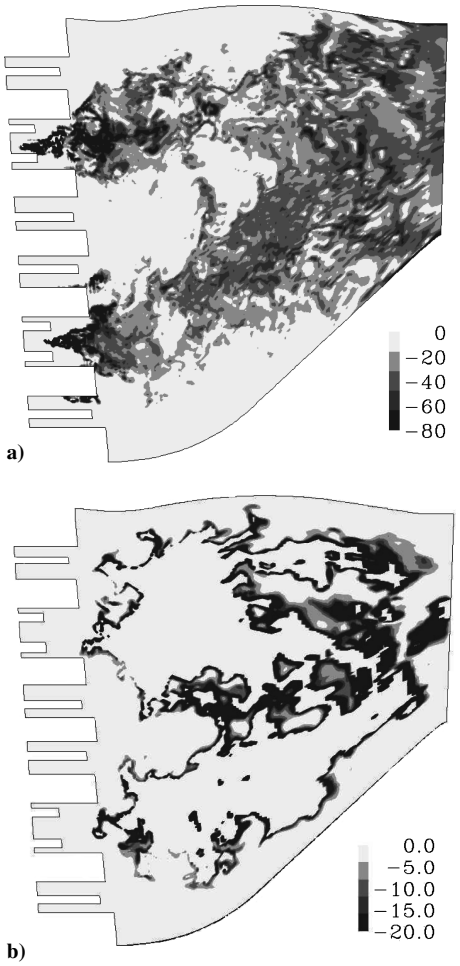

Fig. 19 Reaction-rate contours at the center plane for case 2, GE-2.

a low-velocity zone, thereby allowing time for fuel to vaporize and mix with the air.

All of the recirculation zones and the VBBs are not stationary and undergo oscillation in the axial direction. The larger VBB for the bottom cup also shows some lateral oscillation. It is possible that this motion might be contributing partly to cause the lifted flame structure in the LEMLES results. However, this lateral motion is not considered a major factor because it also exists in the EBULES test cases, and as we have seen, in the EBULES case, the flame remains anchored within the inlet.

Figures 19a and 19b show, respectively, the EBULES and LEMLES reaction rate for the kerosene fuel in GE-2, case 2. For LEMLES, we average the subgrid reaction rates in each LES cell to obtain the LES filtered quantity. It can be see that the EBULES shows distributed regions of burning with a peak in the inlet. Closer examination shows that the mixing time is smaller than the chemical time inside the primary inlets, whereas in the dump region it is much larger. Thus, the flame ignites inside the inlet because EBU has no mechanism to restrict combustion in high-strain-rate regions. On the other hand, the LEMLES simulates the molecular mixing process in addition to the actual chemical rates within the LEM domain. Mixing must complete before ignition, and this delay shifts the ignition to region further downstream, where the strain effects have decreased considerably.

The LES-filtered reaction rate shows a different structure with a majority of the burning occurring in thin regions (reminiscent of flamelet burning). However, there are also regions adjacent to these thin regions where reaction rate is more distributed. Analysis of the local conditions show that thin-reaction zones, distributed reaction zones, and nonpremixed zones coexist in the combustor. The LEMLES approach appears capable of capturing these coexisting regions without requiring any model adjustments. As noted earlier, this capability is essential for capturing the dynamics near LBO.

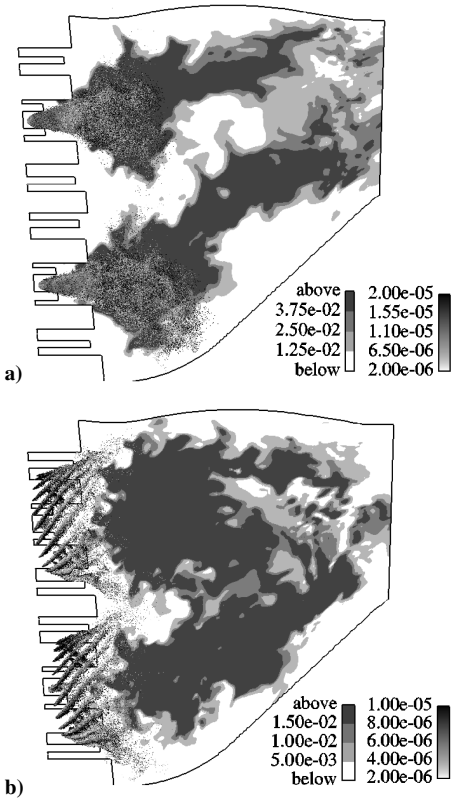

Fig. 20 Spray and CO_2 contours in GE-2.

Finally, Figs. 20a and 20b show, respectively, instantaneous visualization of the spray and CO_2 contours for cases 1 and 2. It can be seen that the spray features are quite different between the two cases. The case 1 spray is primarily a single injector spray from the center of both cups. It can be seen that the spray penetrates considerably into the combustor. CO_2 forms wherever fuel has evaporated and burning occurs. For case 2, the spray is dominated by the injection around the outer rim of the inlet cup. Ignition is delayed because of high strain in the spray vaporizing region, and CO_2 forms just downstream of primary spray mixing region. It can be seen that even though case 2 condition injects more fuel, the mixing regions around the VBB provide ample time to allow nearly all of the droplets to vaporize and mix. Thus, nearly all of the droplets have vaporized within a short distance from the dump plane. Compared to case 1, case 2 is burning more fuel faster and more efficiently. This is as expected for a full power operation, and the current study shows that LEMLES can capture this feature correctly.

To understand how vortex-flame interactions occur and how this process can impact the acoustic fluctuations and combustion dynamics near LBO and combustion instability, additional postprocessing of the results is required. Some results of this type of analysis were reported recently.[24] It appears that for the conditions just simulated, combustion is relatively stable, and no instability is observed. Because the test conditions were chosen for stable operation, this observation is encouraging.

Conclusions

Simulations of spray combustion in sector rigs under different operating conditions are conducted using LES. The current methodology attempts to capture not only spray-turbulence interactions, but also the subgrid fuel–air mixing and finite-rate kinetics occurring at scales below the LES resolution. Reduced finite-rate kinetics for n-heptane and kerosene fuels are used in these studies to predict pollutant emission. Results show that the swirling flow in realistic two-cup combustor sector causes a complex vortex breakdown process and creates multiple recirculation regions for flame stabilization. Because of the shape of the combustor, significant three-dimensional effects are apparent with no similarity between flame structure, VBBs, and outflow variations between the two cups. Spray

combustion is quite efficient during full-power operation because of the distributed injection process. It is also shown that in the LEMLES approach, flame stabilization is more physical and the flame anchors downstream of the dump plane. In contrast, in EBULES the flame resides inside the inlet, which is unphysical.

The current study, along with past applications, has demonstrated that LEMLES can be used for a wide range of conditions without requiring any model adjustment. However, the LEMLES approach is computationally more expensive than EBULES, primarily because of the finite-rate kinetics evaluation within every subgrid cell. Because finite-rate kinetics might have to be included in order to predict LBO and pollutant emission, techniques such as ISAT are being implemented to reduce the overall cost of LEMLES. Application of LEMLES to LBO is the eventual goal of the current research and is currently under investigation.

Acknowledgment

This work was supported by General Electric Aircraft Engine Company under a University Strategic Alliance program.

References

[1]Mongia, H. C., Gore, J. P., Grinstein, F. F., Gutmark, E. J., Jeng, S.-M., McDonell, V. G., Menon, S., Samuelsen, G. S., Santavicca, D., and Santoro, R. J., "Combustion Research Needs for Helping Development of Next Generation Advanced Combustors," AIAA Paper 01-3853, 2001.

[2]Kendrick, D. W., Bhargave, A. B. C. M., Sowa, A. W., Maloney, D. J., and Casleton, K. H., "NOx Scaling Characteristics for Industrial Gas Turbine Fuel Injectors," American Society of Mechanical Engineers, Paper 2000-GT-0098, ASME Turbo Expo, Munich, May 2000.

[3]Eggenspieler, G., and Menon, S., "Combustion and Emission Modeling near Lean Blow-Out in Gas Turbine Engines," *Progress in Computational Fluid Dynamics*, Vol. 5, No. 6, 2005, pp. 281–297.

[4]Candel, S. M., "Combustion Dynamics and Control: Progress and Challenges," *Proceedings of the Combustion Institute*, Vol. 29, 2002, pp. 1–28.

[5]Eggenspieler, G., and Menon, S., "Modeling Pollutant Formation near Lean Blow-Out in Gas Turbine Engines," *Recent Advances in Direct and Large-Eddy Simulations*, Kluwer Academic, Boston, 2003, pp. 351–358.

[6]Eggenspieler, G., and Menon, S., "LES of Premixed Combustion and Pollutant Emission in a DOE-HAT Combustor," *Journal of Propulsion and Power*, Vol. 20, No. 6, 2004, pp. 1076–1086.

[7]Peters, N., *Turbulent Combustion*, Cambridge Univ. Press, Cambridge, England, U.K., 2000.

[8]Kerstein, A. R., "Linear-Eddy Model of Turbulent Transport II," *Combustion and Flame*, Vol. 75, March 1989, pp. 397–413.

[9]Menon, S., and Kerstein, A. R., "Stochastic Simulation of the Structure and Propagation Rate of Turbulent Premixed Flames," *Proceedings of the Combustion Institute*, Vol. 24, 1992, pp. 443–450.

[10]Menon, S., McMurtry, P., and Kerstein, A. R., "A Linear Eddy Mixing Model for Large Eddy Simulation of Turbulent Combustion," *LES of Complex Engineering and Geophysical Flows*, edited by B. Galperin and S. Orszag, Cambridge Univ. Press, Cambridge, England, U.K., 1993, pp. 287–314.

[11]Chakravarthy, V., and Menon, S., "Linear-Eddy Simulations of Reynolds and Schmidt Number Dependencies in Turbulent Scalar Mixing," *Physics of Fluids*, Vol. 13, No. 2, 2001, pp. 488–499.

[12]Sankaran, V., and Menon, S., "LES of Scalar Mixing in Supersonic Shear Layers," *Proceedings of the Combustion Institute*, Vol. 30, 2004, pp. 2835–2842.

[13]Menon, S., and Calhoon, W., "Subgrid Mixing and Molecular Transport Modeling for Large-Eddy Simulations of Turbulent Reacting Flows," *Proceedings of the Combustion Institute*, Vol. 26, 1996, pp. 59–66.

[14]Menon, S., "Subgrid Combustion Modeling for Large-Eddy Simulations of Single and Two-Phase Flow," *LES of Complex Transitional and Turbulent Flows*, Kluwer Academic, Boston, 2000, pp. 329–352.

[15]Chakravarthy, V., and Menon, S., "Large-Eddy Simulations of Turbulent Premixed Flames in the Flamelet Regime," *Combustion Science and Technology*, Vol. 162, 2001, pp. 175–222.

[16]Chakravarthy, V., and Menon, S., "Subgrid Modeling of Premixed Flames in the Flamelet Regime," *Flow, Turbulance and Combustion*, Vol. 65, No. 2, 2000, pp. 131–161.

[17]Sankaran, V., and Menon, S., "The Structure of Premixed Flame in the Thin-Reaction-Zones Regime," *Proceedings of the Combustion Institute*, Vol. 28, 2000, pp. 203–210.

[18]Sankaran, V., Porumbel, I., and Menon, S., "Large-Eddy Simulation of a Single-Cup Gas Turbine Combustor," AIAA Paper 2003-5083, 2003.

[19]Sankaran, V., and Menon, S., "Subgrid Combustion Modeling of 3-D Premixed Flames in the Thin-Reaction-Zone Regime," *Proceedings of the Combustion Institute*, Vol. 30, 2004, pp. 575–582.

[20]Menon, S., and Pannala, S., "Subgrid Modeling of Unsteady Two-Phase Turbulent Flows," AIAA Paper 97-3113, 1997.

[21]Menon, S., and Pannala, S., "Subgrid Combustion Simulations of Reacting Two-Phase Shear Layers," AIAA Paper 98-3318, 1998.

[22]Menon, S., "Subgrid Combustion Modeling of Two-Phase Reacting Flows," *IUTAM Symposium on Turbulent Mixing and Combustion*, Kluwer Academic, Boston, 2001.

[23]Sankaran, V., and Menon, S., "Alignment Statistics and Small-Scale Structures in Swirling Spray Combustion," *Proceedings of the Combustion Institute*, Vol. 29, 2002, pp. 577–584.

[24]Menon, S., "Acoustic-Vortex-Flame Interactions in Gas Turbine Combustors," *Combustion Instabilities in Gas Turbine Engines: Operational Experience, Fundamental Mechanisms, and Modeling*, edited by T. Lieuwen, Vol. 210, Progress in Aeronautics and Astronautics, AIAA, Reston, VA, 2005.

[25]Faeth, G. M., "Mixing, Transport and Combustion in Sprays," *Progress in Energy and Combustion Science*, Vol. 13, No. 4, 1987, pp. 293–345.

[26]Erlebacher, G., Hussaini, M. Y., Speziale, C. G., and Zang, T. A., "Toward the Large-Eddy Simulation of Compressible Turbulent Flows," *Journal of Fluid Mechanics*, Vol. 238, 1992, pp. 155–185.

[27]Schumann, U., "Subgrid Scale Model for Finite Difference Simulations of Turbulent Flows in Plane Channels and Annuli," *Journal of Computational Physics*, Vol. 18, Aug. 1975, pp. 376–404.

[28]Menon, S., Yeung, P.-K., and Kim, W.-W., "Effect of Subgrid Models on the Computed Interscale Energy Transfer in Isotropic Turbulence," *Computers and Fluids*, Vol. 25, No. 2, 1996, pp. 165–180.

[29]Kim, W.-W., and Menon, S., "An Unsteady Incompressible Navier–Stokes Solver for Large Eddy Simulation of Turbulent Flows," *International Journal for Numerical Methods in Fluids*, Vol. 31, No. 6, 1999, pp. 983–1017.

[30]Kim, W.-W., Menon, S., and Mongia, H. C., "Large-Eddy Simulation of a Gas Turbine Combustor Flow," *Combustion Science and Technology*, Vol. 143, No. 1, 1999, pp. 25–62.

[31]Liu, S., Meneveau, C., and Katz, J., "On the Properties of Similarity Subgrid-Scale Models as Deduced from Measurements in a Turbulent Jet," *Journal of Fluid Mechanics*, Vol. 275, 1994, pp. 83–119.

[32]Lilly, D. K., "A Proposed Modification of the Germano Subgrid-Scale Closure Method," *Physics of Fluids A*, Vol. 4, No. 3, 1992, pp. 633–635.

[33]Germano, M., Piomelli, U., Moin, P., and Cabot, W. H., "A Dynamic Subgrid-Scale Eddy Viscosity Model," *Physics of Fluids A*, Vol. 3, No. 11, 1991, pp. 1760–1765.

[34]Schumann, U., "Realizability of Reynolds-Stress Turbulence Models," *Physics of Fluids*, Vol. 20, No. 5, 1977, pp. 721–725.

[35]Patel, N., Stone, C., and Menon, S., "Large-Eddy Simulations of Turbulent Flow over an Axisymmetric Bump," AIAA Paper 2003-0967, 2003.

[36]Fureby, C., Alin, N., Wikstrom, N., Menon, S., Svanstedt, N., and Persson, L., "On Large Eddy Simulation of High Reynolds Number Wall Bounded Flows," *AIAA Journal*, Vol. 42, No. 3, 2004, pp. 457–469.

[37]Fureby, C., and Möller, S.-I., "Large-Eddy Simulation of Reacting Flows Applied to Bluff Body Stabilized Flames," *AIAA Journal*, Vol. 33, No. 12, 1995, pp. 2339–2347.

[38]Pope, S., "Computationally Efficient Implementation of Combustion Chemistry Using In-Situ Adaptive Tabulation," *Combustion Theory and Modelling*, Vol. 1, No. 1, 1997, pp. 41–63.

[39]Smith, T., and Menon, S., "One-Dimensional Simulations of Freely Propagating Turbulent Premixed Flames," *Combustion Science and Technology*, Vol. 128, No. 1, 1996, pp. 99–130.

[40]Pope, S. B., "PDF Methods for Turbulent Reactive Flows," *Progress in Energy and Combustion Science*, Vol. 11, No. 2, 1985, pp. 119–192.

[41]Westbrook, C. K., and Dryer, F. L., "Simplified Reaction Mechanisms for the Oxidation of Hydrocarbon Fuels in Flames," *Combustion Science and Technology*, Vol. 27, No. 1, 1981, pp. 31–43.

[42]Li, S. C., and Williams, F. A., "Reduced Reaction Mechanism for Methane-Air Combustion," *Combustion and Flame*, Vol. 119, No. 3, 1999, pp. 397–413.

[43]Fureby, C., and Löfström, C., "Large-Eddy Simulations of Bluff Body Stabilized Flames," *Proceedings of the Combustion Institute*, Vol. 27, 1994, pp. 1257–1264.

[44]Colby, J., Jagoda, J., and Menon, S., "Flow Field Measurements in a Swirling Spray Combustor," AIAA Paper 2005-4143, 2005.

[45]Mongia, H. C., "TAPS—A 4th Generation Propulsion Combustor Technology for Low Emissions," AIAA Paper 2003-2657, 2003.

[46]Peskin, C., "The Immersed Boundary Method," *Acta Numerica*, Vol. 11, Jan. 2002, pp. 479–517.

[47]Kim, W.-W., and Menon, S., "Numerical Simulations of Turbulent Premixed Flames in the Thin-Reaction-Zones Regime," *Combustion Science and Technology*, Vol. 160, Nov. 2000, pp. 119–150.

N.-S. Liu
Guest Editor